Monazite as a monitor of melting, garnet growth and feldspar recrystallization in continental lower crust

G. DUMOND, 1* P. GONCALVES, 2 M. L. WILLIAMS 3 AND M. J. JERCINOVIC 3

ABSTRACT

Monazite is a common accessory phase in felsic granulite ribbon mylonites exposed in the Upper Deck domain of the Athabasca granulite terrane, western Canadian Shield. Field relationships, bulk rock geochemistry and phase equilibria modelling in the Na₂O-CaO-K₂O-FeO-MgO-Al₂O₃-SiO₂-H₂O-TiO₂-Fe₂O₃ system are consistent with the garnet-rich rocks representing the residual products of ultrahigh temperature melting of biotite-bearing paragneisses driven by intraplating of mafic magma in continental lower crust. The c. 2.64-2.61 Ga Y-rich resorbed monazite cores included in garnet are interpreted as relicts of detrital grains deposited on the Earth's surface after c. 2.61 Ga. Yttrium-poor monazite domains in garnet are depleted in Sm and Gd and linked to fluid-absent melting of biotite + plagioclase + quartz ± sillimanite during a prograde loading path from ≤0.8 to ≥1.4 GPa. The c. 2.61–2.55 Ga Y-depleted, Th-rich monazite domains crystallized in the presence of garnet + ternary feldspar \pm orthopyroxene + peraluminous melt. The c. 2.58–2.52 Ga monazite rims depleted in Th + Ca and enriched in Eu are linked to localized melt extraction synchronous with growth of high-pressure (HP) grossular-rich garnet at the expense of plagioclase during crustal thickening, culminating at >950 °C. Re-heating and dextral transpressive lower crustal reactivation at c. 1.9 Ga resulted in syn-kinematic growth of (La + Ce)-enriched monazite and a second generation of garnet, concurrent with recrystallization of feldspar and orthopyroxene at 1.0-1.2 GPa and 600-700 °C. Monazite grains in this study are marked by positive Eu-anomalies relative to chondrite. A direct link is implied between Y, Sm, Eu and Gd in monazite and two major phases in continental lower crust: garnet and plagioclase. Positive Eu-anomalies in lower crustal monazite associated with modally abundant garnet appear to be directly related to Eu-enrichment and depletions of Y, Sm and Gd that are consequences of garnet growth and plagioclase breakdown during HP melting of peraluminous bulk compositions.

Key words: continental crust; garnet; granulite; monazite; partial melting.

INTRODUCTION

Partial melting is a fundamental mechanism for weakening and differentiating continental crust. Fluid-absent partial melting of biotite-bearing quartzofeldspathic gneisses, in particular, represents one important process for generating granitic melts and their complementary dense garnetiferous residues (Clemens & Vielzeuf, 1987; Rudnick, 1992; Vielzeuf & Montel, 1994; Clemens, 2006; Johnson et al., 2008). Partial melting also leads to strain localization, melt-enhanced deformation and dramatic changes in crustal rheology (Hollister & Crawford, 1986; Brown & Solar, 1998; Searle, 2013; Yakymchuk & Brown, 2014a). Models for crustal-scale channel flow rely on 'melt weakening' to facilitate the necessary drop in viscosity and bulk rheology for crustal flow (Beaumont et al., 2001, 2004; Rosenberg & Handy, 2005).

*This manuscript is dedicated to the memory of Professor J. A. Grambling (1953–1993).

The ability to accurately date the processes involved with weakening and differentiating continental crust requires knowledge of the reactions leading to growth or dissolution–precipitation of accessory phases during and after partial melting. This study explores links between monazite and fluid-absent melting of biotite in continental lower crust, including the production of garnetiferous residues and feldspar recrystallization.

Three approaches have been applied to understanding the monazite + melt system. Monazite solubility during melting has been investigated experimentally (Montel, 1986, 1993; Rapp & Watson, 1986; Rapp et al., 1987; Skora & Blundy, 2012; Stepanov et al., 2012; Xing et al., 2013). Recent theoretical work has focused on thermodynamic forward modelling of common bulk compositions to investigate the growth and dissolution of monazite in meltbearing systems (Kelsey et al., 2008; Yakymchuk & Brown, 2014b). The third approach involves the study of monazite composition and texture in natural

¹Department of Geosciences, University of Arkansas, Fayetteville, AR 72701, USA (gdumond@uark.edu)

²UMR 6249 Chrono-Environnement, Université de Franche-Comté, 16 route de Gray, 25030 Besancon, France

³Department of Geosciences, University of Massachusetts, Amherst, MA 01003, USA

systems, e.g. migmatites, leucogranites and granulites (Watt, 1995; Pyle & Spear, 2003; Goncalves *et al.*, 2004; Kelly *et al.*, 2006; Rubatto *et al.*, 2006; Dumond *et al.*, 2008, 2010; Crowley *et al.*, 2009; Martins *et al.*, 2009; Reno *et al.*, 2012; Lederer *et al.*, 2013; Yakymchuk *et al.*, 2015, among others). We use monazite in high-pressure (HP) peraluminous felsic granulite paragneisses to investigate deep crustal partial melting and post-melting crustal evolution.

Monazite is a common accessory phase in felsic granulite ribbon mylonites exposed in the >400 km² Upper Deck domain of the Athabasca granulite terrane, one of the Earth's largest exposures of continental lower crust (>20,000 km²), in the western Canadian Shield. Felsic granulite paragneisses in the ~10 km thick Upper Deck are inferred to represent the residual products of ultrahigh temperature (UHT) melting of continental lower crust (Snoevenbos et al., 1995; Baldwin et al., 2006). High-resolution X-ray mapping, in situ high-precision electron probe microanalysis (EPMA), major and trace element geochemistry, and phase equilibria modelling reveal first-order links between composition, microstructure, Th-U-total Pb monazite geochronology, and felsic granulite petrogenesis. These links provide tighter

constraints on the evolution of continental lower crust during partial melting, crustal flow, crustal thickening and strain partitioning.

GEOLOGICAL BACKGROUND

Athabasca granulite terrane

The Athabasca granulite terrane is >20,000 km² of continental lower exhumed crust >1.5 GPa ≈ 30 to >55 km paleodepths) exposed north of Lake Athabasca, Canada (Fig. 1a; Dumond et al., 2008; Mahan et al., 2008). The terrane is composed of Archean to Paleoproterozoic mafic and felsic granulites, orthogneisses, paragneisses and minor eclogite bounded on its eastern margin by the 1.85 Ga Legs Lake shear zone (Fig. 1b; Mahan et al., 2003, 2006a,b; Mahan & Williams, 2005). Two main groups of structures have been identified throughout the terrane. The first group (D₁) includes sub-horizontal gneissic fabrics, ESE-trending stretching and intersection lineations and recumbent isoclinal folds (Dumond et al., 2010; Regan et al., 2014). These earliest structures are interpreted to have resulted from granulite facies lower crustal flow at

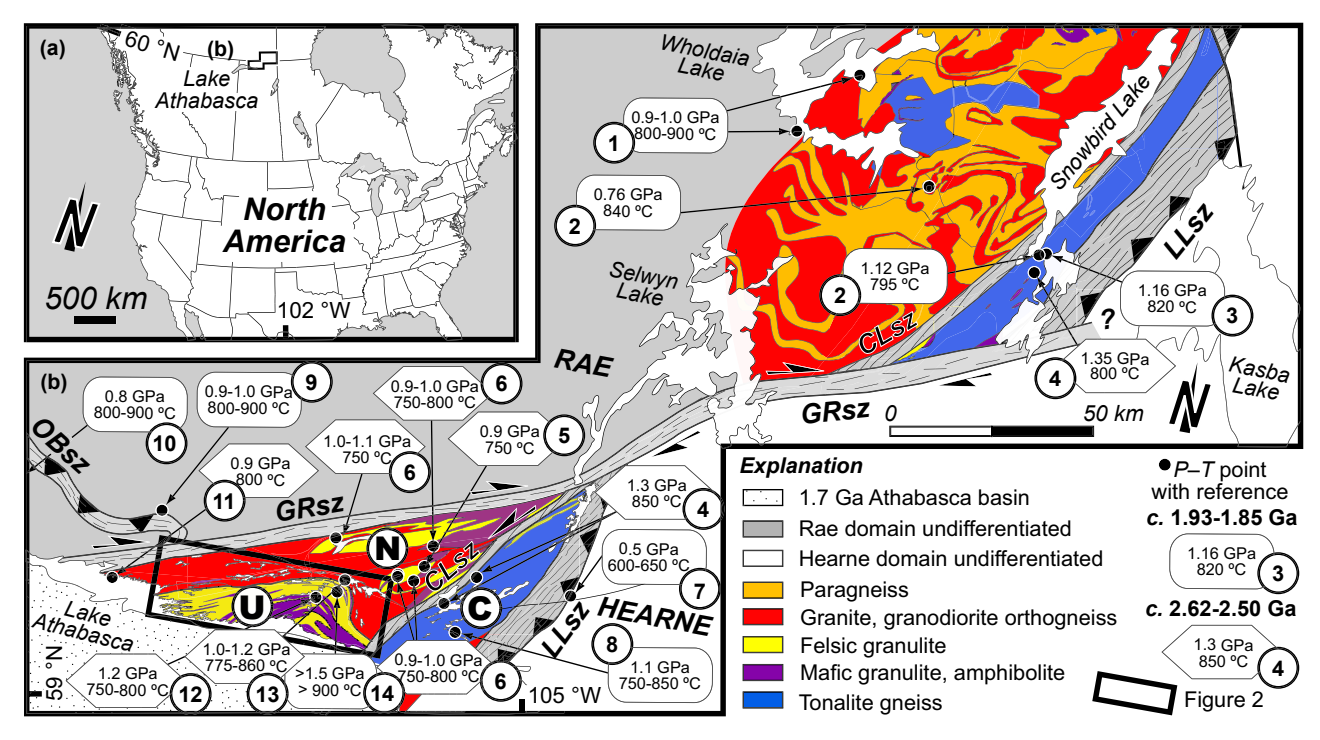


Fig. 1. (a) Location of the Athabasca granulite terrane in North America near the east end of Lake Athabasca. (b) Geological map of the Athabasca granulite terrane with existing *P-T-t* data referenced by number (modified after Mahan *et al.*, 2008; Dumond *et al.*, 2013): (1) Krikorian (2002); (2) Martel *et al.* (2008); (3) Mahan & Williams (2005); (4) Mahan *et al.* (2008); (5) Regan *et al.* (2014); (6) Williams *et al.* (2000); (7) Mahan *et al.* (2003); (8) Williams *et al.* (1995); (9) Williams & Hanmer (2006); (10) Kopf (1999); Williams & Jercinovic (2002); (11) Dumond *et al.* (2010); (12) Kopf (1999); (13) Baldwin *et al.* (2003); (14) Snoeyenbos *et al.* (1995); Baldwin *et al.* (2004). Circled letters correspond to lithotectonic domains within the East Athabasca mylonite triangle mentioned in the text: (C) the Chipman domain, (N) the Northwestern domain and (U) the Upper Deck domain. The rectangle outlines the location of Fig. 2. OBsz, Oldman-Bulyea shear zone; GRsz, Grease River shear zone; CLsz, Cora Lake shear zone; LLsz, Legs Lake shear zone.

2.60–2.55 Ga in the Rae cratonic province (Dumond et al., 2010; Regan et al., 2014). Younger generation structures (D₂–D₅) include SW-dipping gneissic foliations that are overprinted by upright, open to tight folds with localized axial planar and shear foliations, and transposition of folds and gneissic fabrics into sub-vertical to steeply dipping NE-striking mylonitic shear zones (Mahan et al., 2003, 2008; Dumond et al., 2008, 2010, 2013; Martel et al., 2008; Bethune et al., 2013; Regan et al., 2014). All D₂–D₅ structures are attributed to sub-horizontal shortening related to the Taltson and Wopmay orogenies (to the west) and the Trans-Hudson orogeny (to the east) during the interval of 1.94–1.80 Ga (Dumond et al., 2008, 2013; Bethune et al., 2013; Regan et al., 2014).

The East Athabasca mylonite triangle (EAmt; Tantato domain of Slimmon, 1989) is the most thoroughly studied portion of the Athabasca granulite terrane (Hanmer, 1994, 1997). The triangle is divided into three lithotectonic subdomains: Chipman, Northwestern and Upper Deck (C, N and U in Fig. 1b; Hanmer *et al.*, 1994; Williams & Hanmer, 2006; Williams *et al.*, 2009; Mahan *et al.*,

2011). Rocks in the Upper Deck consist of garnetrich felsic granulite, garnetite and paragneisses that are interlayered with sills of mafic granulite and minor eclogite (Fig. 2; Hanmer, 1994, 1997; Snoeyenbos *et al.*, 1995; Baldwin *et al.*, 2003, 2004, 2006, 2007, 2015). The felsic granulite gneisses are characterized by a penetrative mylonitic foliation defined by ribbons of quartz and recrystallized ternary feldspar, in association with Grt + Ky + Rt ± Sil \pm Opx and minor plagioclase (mineral abbreviations after Bucher & Frey, 2002). The typical white colour and mylonitic character of these rocks, informally called the 'white gneisses', were inferred by Snoevenbos et al. (1995) to be analogous to the 'Weiss-stein' granulites from the type locality in the Bohemian Massif (Weiss, 1803; O'Brien & Rötzler, 2003). Minimum peak metamorphic conditions for the felsic granulite gneisses are in the order of 1000 °C at ≥1.5 GPa, assuming equilibrium between ternary feldspar and kyanite (Snoeyenbos et al., 1995).

Geochronology by ID-TIMS (zircon and monazite) and EPMA (monazite) on the felsic granulite gneisses

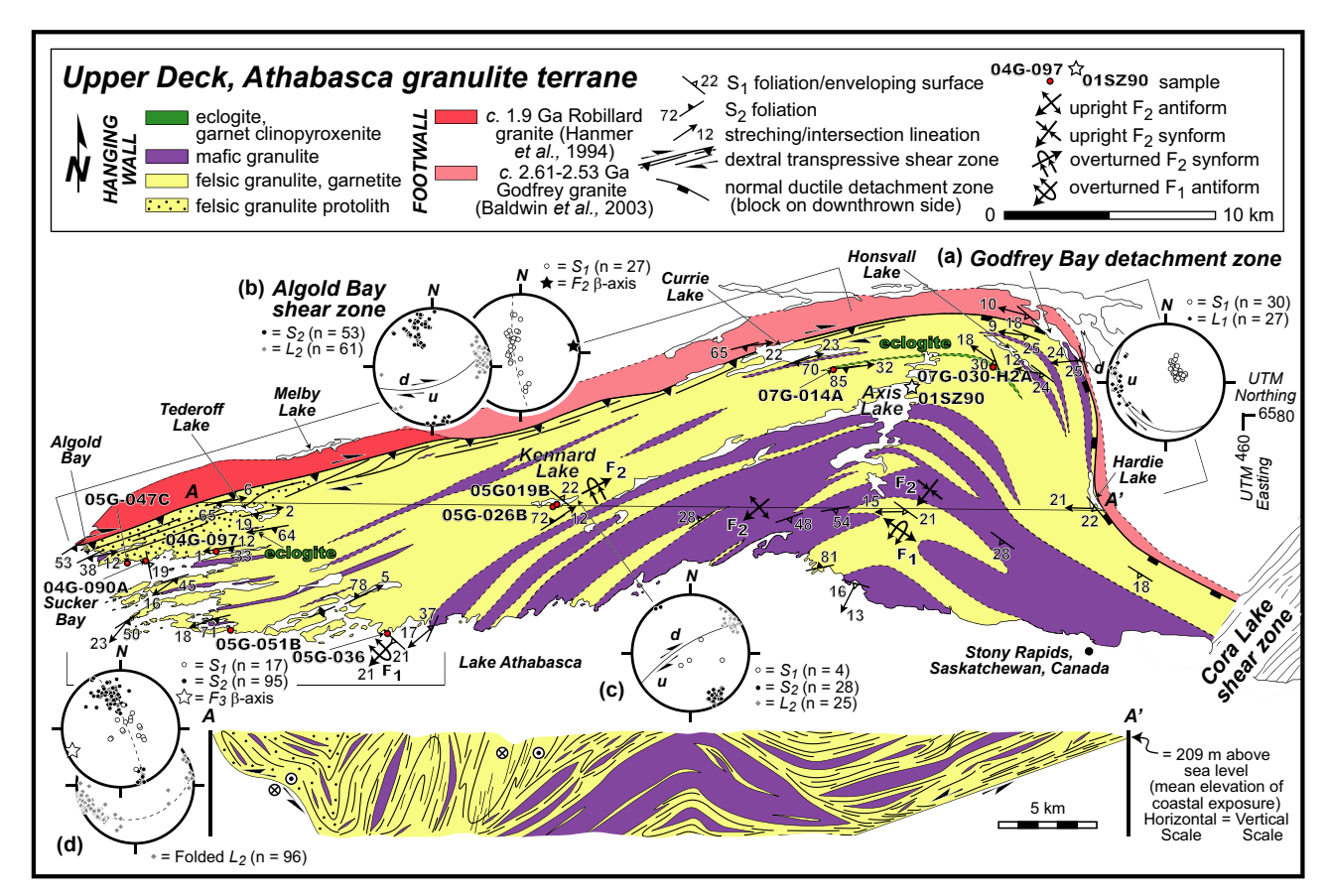


Fig. 2. Simplified geological map and cross-section A–A' of the Upper Deck domain with sample locations (this study; Hanmer, 1994; Baldwin *et al.*, 2003, 2004, 2006). Lower hemisphere equal area projection stereonets are illustrated for structural data from: (a) the Godfrey Bay detachment zone along the northeast boundary of the domain; (b) the Algold Bay shear zone along the northwest boundary of the domain; (c) Kennard Lake; and (d) Sucker Bay and the western portion of the Upper Deck. Open circles are poles to S_1 and filled circles are poles to S_2 . Diamonds correspond to stretching and intersection lineations.

was used to infer an episode of melting and garnet growth at c. 2.55 Ga (Baldwin et al., 2006). Mafic granulite gneisses hosted by the felsic granulite gneisses record temperatures of 890-960 °C and pressures ranging from 1.3 to 1.9 GPa with two populations of U-Pb ID-TIMS zircon dates at c. 2.55–2.52 and c. 1.9 Ga (Baldwin et al., 2003). Eclogite HP metamorphism (1.6 GPa and 750 °C) in the Upper Deck domain has been interpreted at c. 1.9 Ga, based on U-Pb dates obtained in situ via SHRIMP for zircon grains associated with recrystallized clinopyroxene in the eclogite gneisses (Baldwin et al., 2004). However, high-precision single-grain ID-TIMS data for multiple zircon grains from the same rock produced a well-defined discordia between c. 2.54 and 1.90 Ga (sample 01SZ40B in Baldwin et al., 2004).

FIELD RELATIONSHIPS IN THE UPPER DECK DOMAIN

Three main lithologies characterize the Upper Deck domain: (i) sills of abundant mafic granulite and minor eclogite gneisses, (ii) felsic granulite gneisses and (iii) previously unrecognized biotite-bearing paragneisses interpreted to be the protolith to the felsic granulite gneiss (Fig. 2), discussed below. New mapping, combined with data from Hanmer (1994), provides structural context for rocks of the Upper Deck and its tectonic boundaries with the other subdomains of the EAmt (Figs 1b & 2). Rocks in the immediate footwall of the Upper Deck include highstrain orthogneisses represented by the c. 1.9 Ga Robillard granite pluton (Hanmer et al., 1994) and the c. 2.61–2.53 Ga Godfrey granite pluton (Fig. 2; Baldwin et al., 2003).

Lithologies in the western Upper Deck domain

Mafic granulite sills occur throughout the ~10 km thick Upper Deck domain as <1 cm to >1 km-thick lenses composed of Grt + Cpx + Qtz ± Pl ± Hbl gneiss (Fig. 2; see also Baldwin et al., 2003). Folded and transposed layers of minor eclogite (locally >10 m-thick and >10 km in strike-length) are exposed north of Axis Lake and as highly retrogressed boudined lenses (<1 to 2 m-thick) northeast of Sucker Bay (Fig. 2; see also Snoeyenbos et al., 1995; Baldwin *et al.*, 2004, 2007, 2015). The mafic granulite sills are hosted by lithologically heterogeneous stromatic migmatite interpreted to be derived from paragneisses in the southwestern portion of the Upper Deck near Sucker Bay (Figs 2 & 3a-c). The paragneisses become more migmatitic with increasing proximity to the mafic granulite sills, where the paragneisses contain patchy dm-scale neosomes (Fig. 3c) that transition into penetratively deformed layers of garnetite and leucosomes containing garnet and orthopyroxene (Fig. 3c-e). Sills of mafic granulite are intensely veined internally and along their contacts by leucosomes (Fig. 3d). These observations are consistent with partial melting of the paragneisses driven by emplacement of the igneous protolith to the mafic granulite sill complex.

The migmatitic paragneisses in Sucker Bay occur in gradational contact with orthopyroxene-bearing felsic granulite gneisses. These gneisses contain ternary feldspar + Grt + Opx + Qtz + Rt + IIm + Po. Elongate feldspar and quartz ribbons define a penetrative ribbon mylonite gneissic fabric (Fig. 3e). Garnet + orthopyroxene-bearing leucogranites derived from the orthopyroxene-felsic granulites locally crosscut the mafic granulites (Fig. 3f). These felsic gneisses progressively grade along strike and up section into orthopyroxene-absent felsic granulite gneisses composed of ternary feldspar + Grt + Ky \pm Sil + Qtz + Rt + Gr \pm Pl (Fig. 4), similar in character to those previously described by Snoeyenbos *et al.* (1995) and Baldwin *et al.* (2006).

Upper Deck domain boundaries and internal structure

The >400 km², ~10 km thick Upper Deck domain structurally overlies the northwestern domain along a gently SW-dipping, top-to-the-SW ductile shear zone (Hanmer et al., 1994, 1995), here named the Godfrey Bay detachment zone (Fig. 2a). Kinematics defined by recrystallized asymmetric porphyroclasts of orthopyroxene and feldspar define a normal, down-dip to dextral oblique-slip sense of shear (Hanmer et al., 1995). Penetrative ribbon mylonite fabrics of the Godfrey Bay detachment zone merge westwards into the NE-striking, moderately SE-dipping Algold Bay shear zone (Fig. 2). Dextral, SE-side up transpressive kinematics along gently NE-plunging stretching lineations in the shear zone are defined by mm- to cm-scale Opx σ -clasts in Algold Bay and map-scale C-S foliation trajectories in the vicinity of Tederoff Lake (Fig. 2b). The tectonic significance of these two shear zones is the subject of a separate study. The boundary of the Upper Deck domain is cut by the NE-striking, steeply NW-dipping Cora Lake shear zone (Fig. 2; Mahan et al., 2008; Regan et al., 2014). The 3-5 km wide shear zone is defined by ultramylonite fabrics in granulites that record a sinistral normal obliqueslip history along a moderately SW-plunging stretching lineation at c. 1.88 Ga during the early stages of exhumation of the Athabasca granulite terrane (Regan et al., 2014).

All major lithologies in the Upper Deck domain were affected by a D_1 deformation event defined by sub-horizontal to variably gently dipping penetrative ribbon mylonite fabrics (S_1) (Figs 2b–d, 3a & 4a,b). Fabrics associated with D_1 are locally defined by blades of kyanite and layers of garnetite + leucosome (Fig. 4a,b). These observations are most consistent with migmatite generation occurring

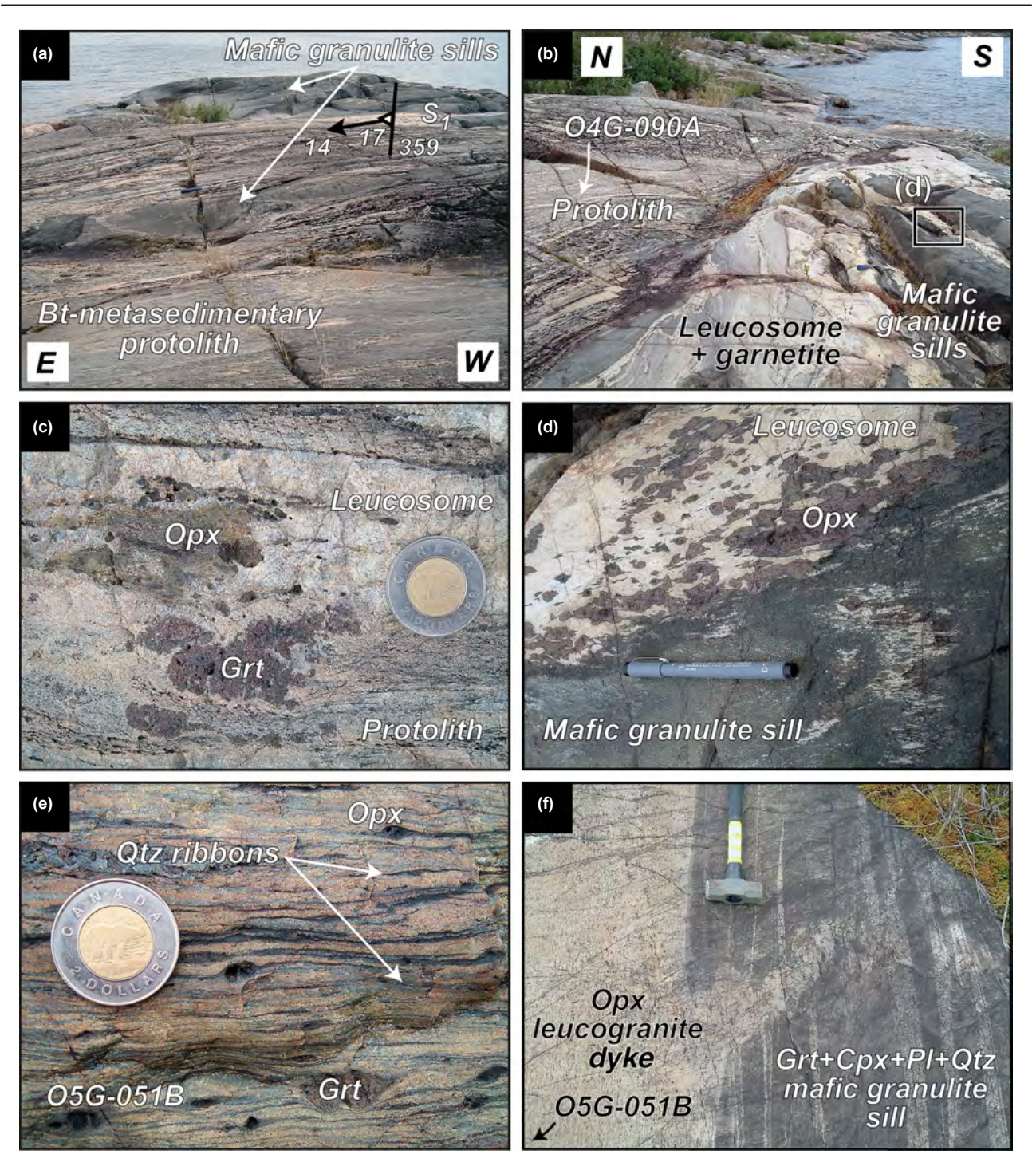


Fig. 3. Outcrop photos of field relationships between the felsic granulite paragneiss protolith, mafic granulite gneisses and Opxbearing felsic granulite gneisses in the western Upper Deck domain near Sucker Bay in Fig. 2. Sample locations are noted by arrows with sample numbers. (a) Outcrop of metre-scale, mafic granulite sills hosted by Bt-bearing paragneiss protolith. All gneisses in the outcrop are penetratively deformed by a gently dipping S_1 ribbon mylonite fabric. (b) Close-up view towards east of mafic granulite sills in the background of picture in (a). Note the contact zone between the Bt-bearing paragneiss protolith and mafic granulite sills (dipping $<25^{\circ}$ to viewer's right) and the abundance of leucosome and garnetite pods in the contact zone. (c) Biotite-paragneiss protolith near mafic granulite with Grt + Opx neosome. (d) Close-up view of Opx-bearing leucosome layers and cross-cutting veins in the mafic granulite sills in (b). (e) Characteristic ribbon mylonite fabric in the Opx-bearing felsic granulite defined by ribbons of Qtz + ternary feldspar and elongate clasts of Opx + Grt. (f) Leucogranite dyke derived from Opx-felsic granulite that cross-cuts a mafic granulite sill and has apophyses that intrude parallel to layering in the sill.

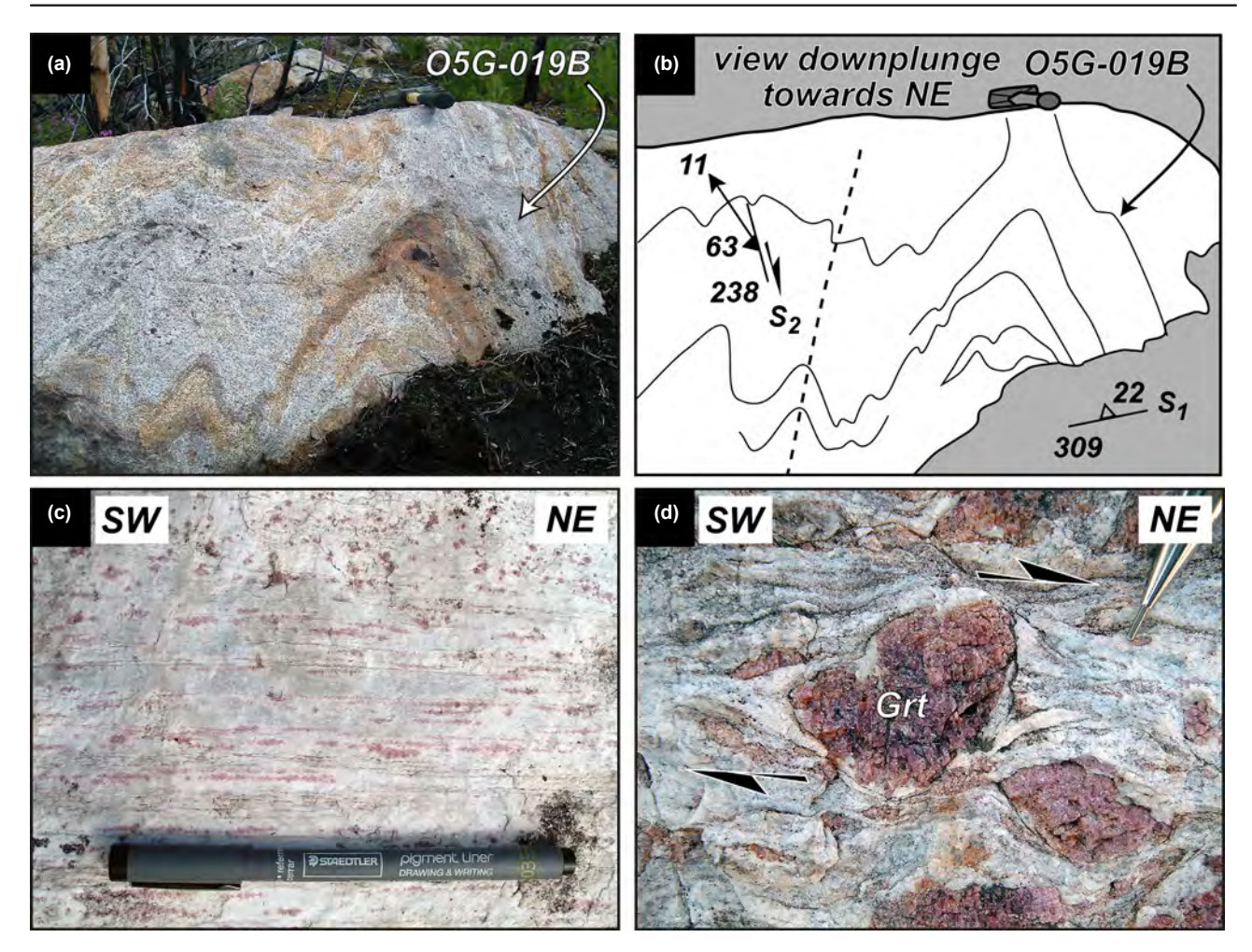


Fig. 4. Outcrop photos of aluminosilicate-bearing (Opx-absent) felsic granulites in the western Upper Deck domain near Kennard Lake (see Fig. 2 for location). (a) and (b) Outcrop and sketch of Grt + Ky + Sil felsic granulite ribbon mylonite. Note the early NW-striking S_1 fabric defined by leucosomes + layers of garnetite with an enveloping surface similar in orientation to S_1 fabrics observed in Sucker Bay (Fig. 3a). The outcrop is overprinted by a penetrative, steeply NW-dipping S_2 cleavage. Note location of sample 05G-019B for this study. (c) Outcrop of fine-grained felsic granulite with a penetrative D_2 ultramylonite fabric defined by ribbons of quartz and feldspar. Note apparent grain-size reduction in garnet. (d) View parallel to the stretching lineation and perpendicular to the foliation (XZ-plane of strain). Note mantled garnet δ -clast with recrystallized tails of plagioclase defining dextral sense of shear.

synchronous with the S_1 sub-horizontal fabric. Deformation during D₂ involved transposition of these gneissic mylonite fabrics into overturned tight to isoclinal folds (F₂) associated with NE-striking steeply dipping to sub-vertical foliations (S₂) and well-developed variably plunging intersection and stretching lineations (L₂; Figs 2b–d & 4b). The D₂ event is also associated with zones of sub-vertical NE-striking S₂ ultramylonite fabrics with gently NE-plunging stretching lineations (L₂) defined by ribbons of quartz and feldspar (Fig. 4c). Dextral kinematics observed parallel to L2 and perpendicular to S2 are defined by mantled garnet and orthopyroxene porphyroclasts (Figs 3e, 4d & 5c). All S_1 and S_2 fabrics, in addition to L_2 lineations and F2 fold axes, were subsequently folded during a D_3 event (Fig. 2d).

MICROSTRUCTURE, PETROGRAPHY AND MINERAL COMPOSITIONS

Nine samples were chosen from a suite of over 70 samples of felsic granulite and paragneiss protolith rocks collected along a 20 km-long transect in the western portion of the Upper Deck (between Sucker Bay and Kennard Lake) and in the vicinity of Honsvall Lake (as identified in Fig. 2; for reference, felsic granulite sample 01SZ90 from Baldwin et al., 2006; is plotted as a star in Fig. 2). Wholerock geochemistry for eight of the samples is summarized in Table S1 and discussed below. Three samples were chosen for detailed microanalysis. Sample 04G-097 is an orthopyroxene-bearing felsic granulite ribbon mylonite containing a penetrative gently SE-dipping S1 foliation and SW-plunging

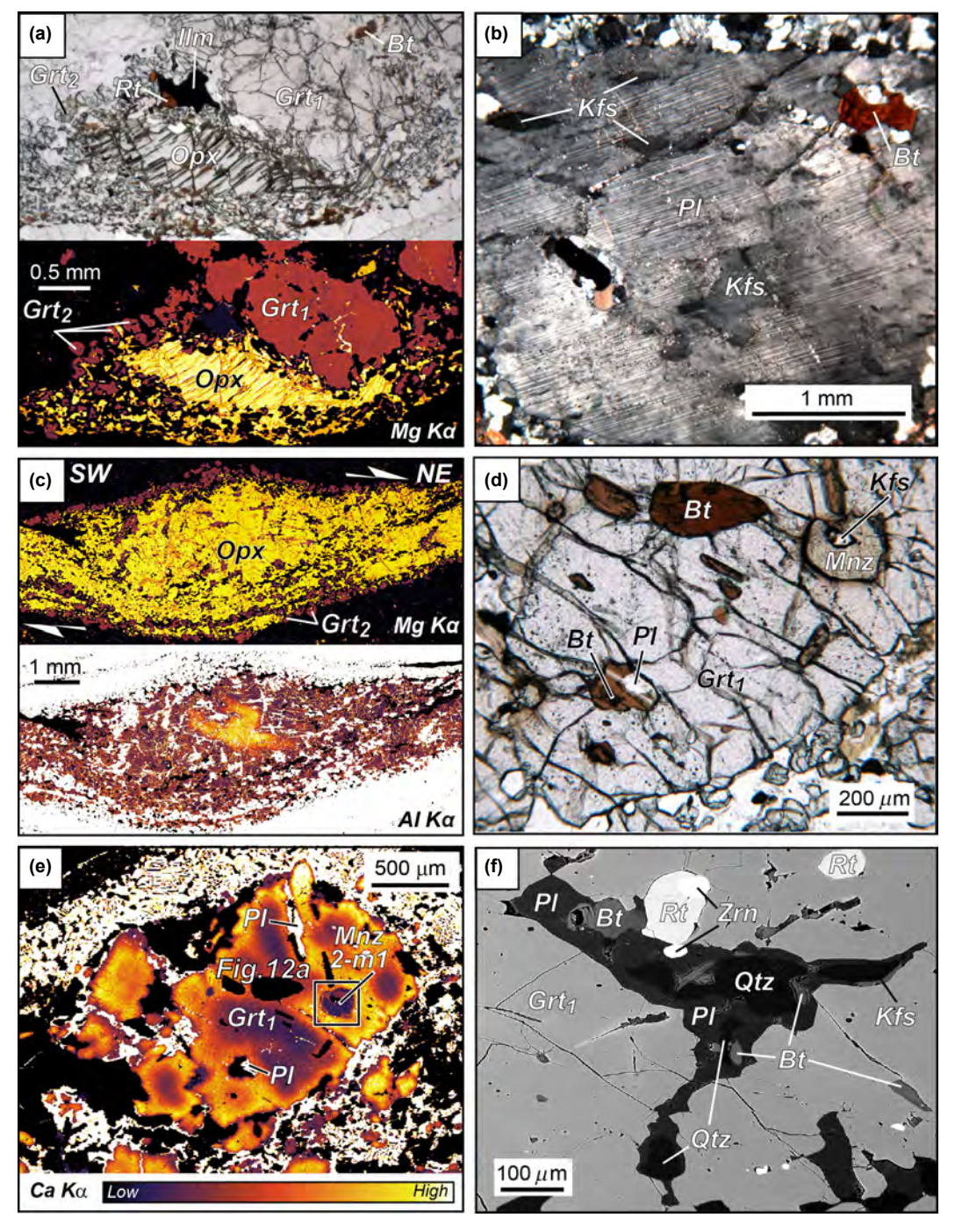


Fig. 5. Microstructures and X-ray compositional maps for sample 04G-097. (a) Photomicrograph (plane-polarized light) and Mg $K\alpha$ map of peak assemblage in Opx-bearing felsic granulite: Opx + Grt₁ + Qtz + Rt + ternary feldspar. Ilmenite is a matrix phase that was not observed in garnet. (b) Large anti-perthite (ternary feldspar) porphyroclast with resorbed Ti-rich biotite inclusion. (c) High-resolution X-ray maps of recrystallized orthopyroxene for Al $K\alpha$ and Mg $K\alpha$. Note corona of Grt₂ around orthopyroxene in Mg $K\alpha$ map and diffuse high-Al core in Al $K\alpha$ map. (d) Large poikilitic porphyroblast of Grt₁ with inclusions of Bt + Pl + Qtz + Mnz + Zrn + Rt. (e) High-resolution Ca Kα X-ray map of garnet depicted in (d). Note recrystallized ternary feldspar matrix above garnet. Garnet porphyroblasts are characterized by low-grossular cores surrounded by high-grossular annuli. Note location of monazite 04G-097-2-m1 in high-grossular Grt₁ (illustrated in Fig. 12a). (f) Backscattered electron image of poly-phase inclusion of Bt + Pl + Qtz + Kfs + Zrn + Rt in high-grossular Grt₁ annulus.

stretching lineation defined by ribbons of quartz + feldspar. This sample was chosen to constrain peak metamorphic conditions, model the P-T evolution of the felsic granulites, and texturally link these results to monazite composition and geochronology. As mentioned previously, the orthopyroxene-felsic granulites gradationally transition into Sil + Ky-bearing and garnet-rich felsic granulites and garnetite that lack orthopyroxene. An oriented sample (05G-019B) of the kyanite-rich felsic granulite was collected from the outcrop depicted in Fig. 4a,b to constrain the P-T conditions and age of garnet growth and partial melting indicated by the leucosomes and garnetite layers that define the early S_1 fabric. Metre-scale, sub-vertical ultramylonite zones are abundant in the kyanite-bearing felsic granulites (Fig. 4c). The third sample (05G-026B) is from a D_2 dextral ultramylonite zone to constrain the timing of D_2 strain and the potential relationship between monazite growth and feldspar recrystallization.

High-resolution X-ray mapping of silicate phases was carried out prior to analysis with the Cameca® SX50 EPMA at the University of Massachusetts-Amherst. Maps were generated at 15 kV and 150–200 nA with 4–10 μ m pixel step sizes and 50–100 ms dwell times. Quantitative analyses, guided by the X-ray maps, were collected at 15 kV and 20 nA with a focused beam for garnet and orthopyroxene and a defocused beam (5 μ m diameter) for biotite and plagioclase (Table S2). Count times were 20 s on peak and 10 s on background. Calibrations were made using common natural and synthetic standards.

Orthopyroxene-bearing felsic granulite (sample 04G-097)

Major phases in the orthopyroxene-bearing felsic granulites are garnet, orthopyroxene, ternary feldspar (as perthite and anti-perthite), biotite, quartz and minor plagioclase (Fig. 5a-c). The main penetrative S₁ fabric is defined by ribbons of quartz, aggregates of garnet, and dynamically recrystallized orthopyroxene, ternary feldspar and biotite. Zircon, monazite, rutile, ilmenite and pyrrhotite are abundant as matrix accessory phases, and all occur as inclusions in garnet (Figs 5d-f & S1), with the notable exception of ilmenite (Fig. 5a). Ternary feldspar (anti-perthite) occurs as large porphyroblasts that locally contain resorbed Ti-rich biotite inclusions (up to 6.25 wt% TiO₂; Table S2) similar to those preserved in garnet (Fig. 5b). Biotite also occurs as a minor matrix phase (Fig. 5a).

Orthopyroxene porphyroclasts (3-10 mm) occur as fractured grains with undulose extinction and have diffuse high-Al cores (up to 4.48 wt% Al₂O₃) and low-Al rims (1.08 wt% Al₂O₃; Fig. 5c; Table S2). Garnet occurs in two microstructural domains. The first occurrence consists of large poikiloblastic grains (1–3 mm) in leucocratic layers with ternary feldspar, (Fig. 5d,e). The and biotite garnet poikiloblasts have grossular-poor cores (Grs₄) and grossular-rich annuli (up to Grs₁₃) near the rims (Fig. 5e; Table S2). The grossular-rich domains are characterized by the occurrence of Ti-rich biotite inclusions (up to 6.07 wt% TiO₂; Table S2). Polyphase inclusions in garnet are common in the grossular-rich garnet domains and include K-feldspar + quartz + plagioclase + biotite + rutile + zircon (Fig. 5f). Plagioclase (An₂₇) also occurs as resorbed grains with biotite as inclusions in grossular-rich garnet (Fig. 5d,e). The second occurrence of garnet consists of small (0.10–0.30 mm) grossular-rich grains (up to Grs₁₆) that, with quartz, define coronae around dynamically recrystallized orthopyroxene porphyroclasts (Fig. 5a,c). Garnet grains that define the corona are typically poikiloblastic with inclusions of plagioclase and quartz.

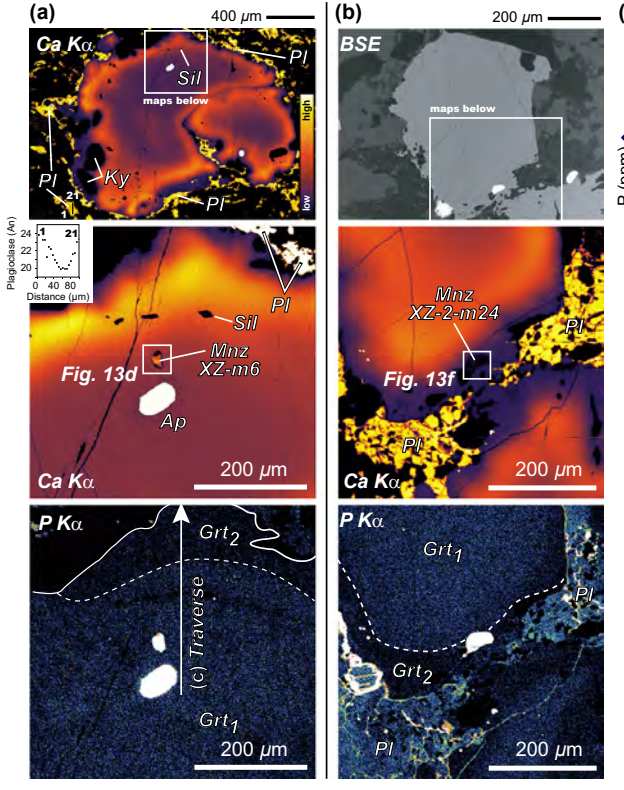
Microstructural observations support growth of Grt_1 , orthopyroxene and ternary feldspar by a fluidabsent biotite melting reaction of the type $Bt + Pl + Qtz \rightarrow Opx + Grt + Kfs + melt$ (e.g. Vielzeuf & Montel, 1994). By contrast, the Grt_2 corona texture around orthopyroxene grains (Fig. 5a,c) may have occurred according to a reaction of the type $Opx + Pl \rightarrow Grt + Otz$.

Sillimanite + kyanite-bearing felsic granulite (sample 05G-019B)

Major phases in the aluminosilicate-bearing felsic granulite gneisses include garnet, ternary feldspar, quartz, kyanite, sillimanite, with minor plagioclase and biotite (Fig. 6). Accessory phases include abundant rutile + monazite + zircon + graphite + apatite. Fluorapatite occurs only as rounded grains (up to $150~\mu m$) included in garnet and is completely absent from the matrix (Fig. 6a).

Elongate quartz ribbons, garnet aggregates, blades of kyanite + sillimanite (up to 1 mm long) and recrystallized ribbons of ternary feldspar define the sub-horizontal to gently dipping S_1 fabric. The upright S₂ foliation is locally defined by fractured aggregates of resorbed garnet with fractures filled by kyanite + sillimanite + quartz + rutile. The textural relationship between kyanite and sillimanite, as observed in the matrix, remains equivocal. However, tens of micron prismatic grains of sillimanite occur as inclusions in garnet that may have nucleated prior to resorbed kyanite inclusions in garnet rims (Fig. 6a). Recrystallized ribbons of quartz + K-feldspar + plagioclase + kyanite + sillimanite also define S₂. Dextral oblique-slip kinematics for D₂ strain are defined by isolated garnet porphyroclasts mantled by recrystallized quartz and plagioclase (Figs 2c, 4d &

Garnet (up to 50% by mode) varies from inclusion-poor to poikilitic with inclusions of sillimanite, kyanite, rounded quartz, monazite, zircon, rutile, graphite and rare rusty brown anhedral biotite (Figs 6a & S2). Garnet cores contain crystallographically oriented needles of rutile, inferred to represent exsolution from a more Ti-rich garnet (Snoeyenbos et al., 1995). Polyphase inclusions near garnet rims are common, and consist of kyanite + K-feldspar + plagioclase + quartz + rutile + zircon (see also



(c) Grt₁ 700 600 500 400 3 G 300 30 200 20 2 10 100 0 -100 150 200 250 300 350 Distance (µm)

Fig. 6. (a) and (b) High-resolution X-ray maps and backscattered electron (BSE) image of garnet in Ky + Sil-bearing felsic granulite 05G-019B illustrating setting of monazite inclusions depicted in Fig. 13. Dashed white line in phosphorous maps marks the boundary between highphosphorous Grt₁ cores and low-phosphorous Grt₂ rims discussed in the text. (c) Quantitative EPMA traverses across the boundary between Grt₁ cores and Grt₂ rims. Grt₁ includes low-Grs garnet cores (Grs₃₋₄) that grade into high-Grs annuli $(Grs_{7-11}).$

Snoeyenbos et al., 1995; Baldwin et al., 2006). Rounded polyphase inclusions of biotite + quartz (up to 0.24 mm) are less commonly present in garnet. Biotite inclusions are rich in Ti (up to 5.42 wt% TiO₂; Table S2). Some quartz grains included in garnet contain inclusions of either graphite or rutile (Fig. S2). Two occurrences of garnet were identified based on trace element maps of phosphorous (Fig. 6a,b), an element interpreted to be relatively unaffected by retrograde diffusion (Spear & Kohn, 1996). The two occurrences of garnet are defined by high-phosphorus (200-300 ppm) cores (Grt₁) and low-phosphorous (<150 ppm) rims (Grt₂; Fig. 6a,b). The sharp contact separating cores from rims is coincident with the occurrence of an ~50 µm wide highgrossular annulus (Grs7-8, locally up to Grs11 and Alm₅₇Pyp₃₂), comparable with the grossular-rich annuli observed in the orthopyroxene-bearing felsic granulite 04G-097 (cf. Fig. 5e with Fig. 6a,b). The interior margin of the annuli (towards the garnet core) locally coincides with small (20–30 µm) prismatic inclusions of sillimanite (Fig. 6a). The exterior margin of the annuli (towards the garnet rim) locally coincides with resorbed inclusions of kyanite (Fig. 6a). The inner core of Grt₁ and the outer rim of Grt₂ display similar low-grossular compositions (Grs₃₋₄, Alm₅₉₋₆₁Pyp₃₅₋₃₆; Fig. 6c). The low-phosphorous Grt₂ rims are locally mantled and intergrown with plagioclase (An₂₀ cores and An₂₃ rims; Fig. 6a,b;

Table S2), recrystallized ternary feldspar + quartz, and/or intergrowths of kyanite \pm rutile.

Observations are most consistent with growth of Grt₁, defined by low-grossular cores and high-grossular annuli, via a fluid-absent partial melting reaction of the type Bt + Pl + Sil + Qtz \rightarrow Grt + Kfs + melt (with Ky present at higher pressures; Tropper et al., 2005). The association and local intergrowth of lowgrossular Grt₂ with secondary plagioclase (Fig. 6b) may represent a low-P assemblage that grew sometime after decompression and partial breakdown of the high-grossular Grt₁ annuli (Snoeyenbos et al., 1995).

Felsic granulite ultramylonite (sample 05G-026B)

Much of the felsic granulite in the western Upper Deck domain is over-printed by metre-scale, steeply dipping D₂ ultramylonite zones (Fig. 4c). Sample 05G-026B is a monazite-bearing felsic granulite from an ultramylonite zone that contains a penetrative, steeply NW-dipping foliation and gently NE-plunging stretching lineation defined by ribbons of ternary feldspar, plagioclase and quartz (Figs 4c & S3). Fractured porphyroclasts of garnet are mantled by recrystallized ribbons of ternary feldspar, plagioclase and quartz that define σ -type geometries and dextral, oblique-slip kinematics (Fig. S3). Elongate monazite grains are aligned sub-parallel to S2, in association with ribbons of ternary feldspar and quartz (Fig. 14a).

WHOLE-ROCK MAJOR AND RARE EARTH ELEMENT GEOCHEMISTRY

Data for whole-rock geochemistry for major and rare earth elements were obtained through Activation Laboratories, Ltd. in Ancaster, Ontario, Canada, with additional whole-rock major element data acquired from the Ronald B. Gilmore XRF Lab at the University of Massachusetts-Amherst (Table S1). The data are combined with data from Baldwin et al. (2006) to characterize the compositional variation in the felsic granulites (Figs S4 & S5); in these figures, sample 04G-090A (Fig. 3b) represents an example of the likely protolith, based on the previously mentioned field observations. The metagraywacke composition (CEVP) used in the partial melting experiments of Vielzeuf & Montel (1994) and the compositions of the Bohemian Massif felsic granulites were included in Fig. S4a,b for comparison (from Fiala et al., 1987; Carswell & O'Brien, 1993; Stípská & Powell, 2005; Tropper *et al.*, 2005). Analysis of major element whole-rock geochemistry. following the approach of Frost et al. (2001), indicates that the Upper Deck felsic granulite bulk comare predominantly magnesian positions peraluminous (Fig. S4a,b; Table S1). The protolith bulk composition (sample 04G-090A) is compositionally similar to the greywacke bulk composition used in the experiments of Vielzeuf & Montel (1994; Fig. S4a,b). Figure S4c illustrates the nearly one-toone rare earth element normalization of the protolith bulk composition relative to average bulk compositions for Late Archean greywacke and Archean cratonic shale (Condie, 1993).

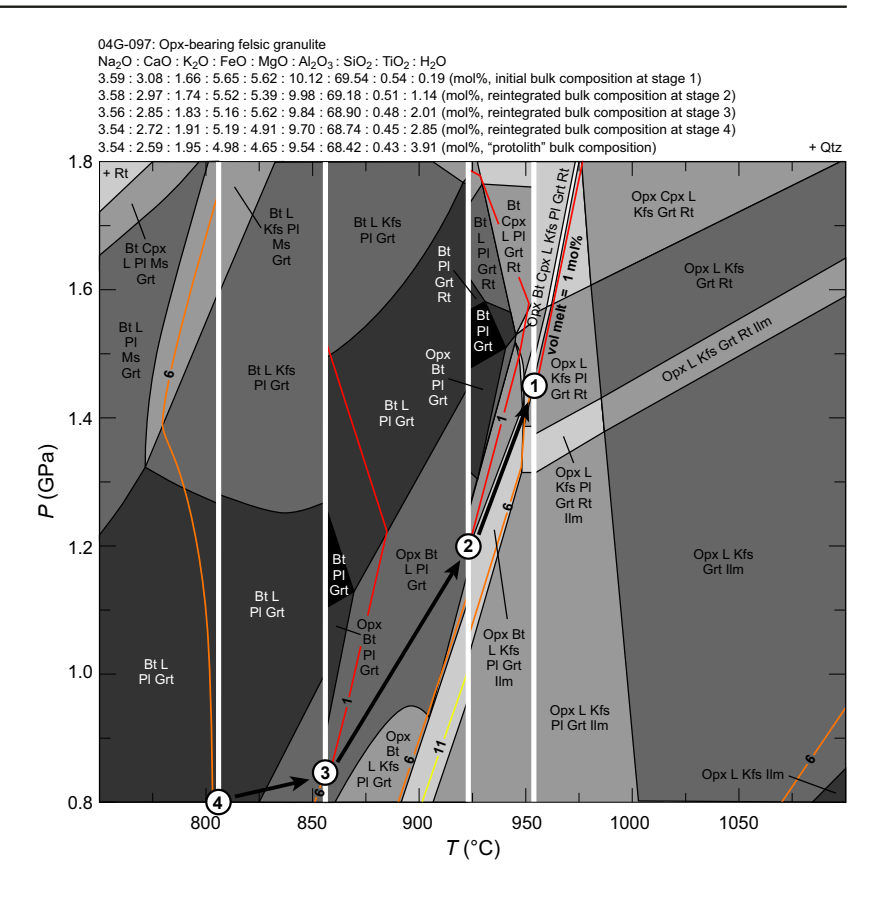
The felsic granulite bulk compositions are quite variable, ranging from magnesian to ferroan and calcic to alkalic-calcic (Fig. S4a,b; Table S1). This variattributed accumulations is to garnet ± orthopyroxene (Fig. S4a,e) and feldspar (Fig. S4b,d) in these residual bulk compositions. The bulk compositions for some of the felsic granulites share characteristics common to leucogranites, including the Opx-leucogranite dyke derived from the felsic granulite that cuts mafic granulite (sample 05G-051B in Fig. 3f; see leucogranite compositional field in fig. S4a,b from Frost et al., 2001). Some of the Opx-bearing felsic granulites have low X_{A1} bulk compositions (e.g. sample 04G-097; $X_{\rm Al}$ < 0.35; Table S1) similar to the Type I Opx-bearing HP felsic granulites identified by Chen et al. (2008). The entire suite of Upper Deck felsic granulites is generally more magnesian, alkaline and silica-poor than the Bohemian Massif felsic granulites (Fig. S4a,b). Rare earth element data normalized to bulk continental crust values from Rudnick & Gao (2003) generally reveal heavy rare earth element (HREE) enrichments and slightly positive Eu-anomalies consistent with garnet and feldspar accumulation respectively (Fig. S5). The Opx-bearing leucogranite dyke, in particular, exhibits a well-developed positive Eu-anomaly in association with the most prominent HREE depletions observed in this data set, indicating it is most likely the residue of a peraluminous melt that fractionated feldspar after it was extracted from a garnet-rich residuum (Figs S4e & S5).

PHASE EQUILIBRIA MODELLING

For the Opx-absent felsic granulite gneiss, Snoeyenbos et al. (1995) estimated UHT conditions ≥1000 °C at ≥ 1.5 GPa based on ternary feldspar thermometry, and assuming equilibrium with kyanite. The reliability of this approach for estimating metamorphic UHT conditions has been questioned by Štípská & Powell (2005) for similar felsic granulites in the Bohemian Massif. Štípská & Powell (2005) argued that the ternary feldspar was a relict of magmatic crystallization rather than metamorphic in origin. Baldwin et al. (2006) adopted a similar interpretation for the Upper Deck felsic granulites, suggesting that the felsic granulites were orthogneisses. However, the REE data for the Upper Deck felsic granulite protolith are consistent with a metasedimentary origin (Fig. S4c). Furthermore, the identification of resorbed Ti-rich biotite inclusions in ternary feldspar from this study supports a metamorphic origin for Upper Deck ternary feldspar, e.g. as a prograde phase resulting from a fluid-absent biotite melting reaction (Fig. 5b; Vielzeuf & Schmidt, 2001). The most common way to establish UHT conditions is via high Mg-Al assemblages like sapphirine + quartz (Goncalves et al., 2004; Kelsey & Hand, 2014; Korhonen et al., 2014). Unfortunately, these assemblages have not been identified in the Upper Deck domain, and most of the widespread felsic granulites have a mineralogy that limits what can be achieved using conventional thermobarometric methods. In this contribution, we use phase equilibria modelling with the bulk composition of the newly discovered orthopyroxene-felsic granulite (sample 04G-097; Figs 7-10; Tables S1-S4) to provide new constraints on this occurrence of UHT metamorphism.

The felsic granulite gneisses of the Upper Deck domain potentially experienced large degrees of partial melting and melt loss, as suggested by abundant quartzofeldspathic leucosomes and garnet-rich layering that define the early S_1 foliation (Figs 3b–e & 4a, b). These residual bulk compositions are suitable for determining the post-melt loss P-T conditions and retrograde evolution of the felsic granulites. However, constraining the prograde history of the felsic granulites and understanding the significance of compositional zoning in garnet and orthopyroxene requires accounting for the effects of melt loss on the bulk composition. The inversion technique of Korhonen

Fig. 7. Melt reintegration model represented as a composite pseudosection computed with Perple_X 6.6.8 for Opxbearing felsic granulite 04G-097. Coloured contours correspond to mol.% melt isopleths. The far right panel corresponds to the P-T pseudosection calculated for the starting residual whole-rock bulk composition in Table S1 + 0.03 wt% H₂O to achieve ~1 mol.% melt at the inferred peak conditions. The four adjacent panels illustrate the effect of melt reintegration into the residual bulk composition such that a melt connectivity threshold of 7 mol.% melt (~7 vol.%) was reached at each stage. See text for discussion. Four melt reintegration stages (numbers 1-4) were performed at the 1 mol.% melt isopleth down pressure and temperature along the hypothetical P-T path depicted in Fig. 8. The final reintegrated bulk composition at stage 4 is inferred to represent a plausible initial (protolith) bulk composition that was used to compute the pseudosection in Fig. 8. The composition of melt and the reintegrated bulk composition for each stage are provided in Table S4.



et al. (2013) was used to recalculate plausible protolith bulk compositions by the stepwise reintegration of melt into the initial residual bulk composition along an inferred prograde P-T path (cf. White et al., 2004). In this context, the two main goals of the phase equilibria modelling are to explore the effect of melt transfer on phase relations and constrain the P-T evolution for the felsic granulite gneisses. Phase relations were then texturally linked to monazite zoning and chemistry to provide geochronological constraints on the evolution of felsic granulite gneisses in continental lower crust (see monazite section below).

Pseudosections were computed in NCKFMASHTO and Na₂O-CaO-K₂O-FeO-MgO-Al₂O₃–SiO₂–H₂O–TiO₂–Fe₂O₃ systems using Perple X 6.6.8 (Connolly, 2005) and the updated 2002 version of the internally consistent thermodynamic data set of Holland & Powell (1998; hp02ver.dat in Perple X; Figs 7–11 & S6). Phases and solution models considered in the modelling included: garnet (White et al., 2007), ternary feldspar (Fuhrman & Lindsley, 1988), orthopyroxene (White & Powell, 2002), clinopyroxene (Green et al., 2007), biotite (Tajčmanová et al., 2009), ilmenite (White et al., 2000), white mica (Coggon & Holland, 2002) and haplogranitic melt (White et al., 2007; Table S3). The amount of H2O used in the modelling for the Opxbearing felsic granulite (04G-097) and Sil + Ky-bearing felsic granulite (05G-019B) bulk compositions was estimated assuming that all loss on ignition reported in Table S1 corresponds to H2O. This amount of H₂O was adjusted for the first stage of the melt reintegration by adding 0.03-0.04 wt% H₂O to ensure that a minimum of 1 vol.% melt was present at the inferred peak conditions, representing the amount of melt that would be retained as thin films along grain boundaries after melt loss (Yakvmchuk & Brown, 2014a; see melt reintegration section below). Although the amount of Fe₂O₃ is a critical compositional variable in modelling Fe + Mg-bearing partially molten systems, the impact on UHT (>950 °C) phase relations in the peraluminous pyrrhotite-bearing (sample 04G-097) and graphite-bearing (sample 05G-019B) systems of this study appears to be limited. This effect was evaluated with $T - X_{\text{Fe}_2\text{O}_3}(X_{\text{Fe}_2\text{O}_3} = \text{Fe}_2\text{O}_3/[\text{FeO} + \text{Fe}_2\text{O}_3])$ sections calculated at 1.45 GPa using the inferred protolith bulk compositions determined after melt reintegration for both samples (Fig. S6; Table S4). The modelling indicates that virtually any addition of Fe₂O₃ to the system will stabilize ilmenite (Fig. S6a). These results are contrary to petrographic observations from Opx-bearing felsic granulite gneisses that document the ubiquitous presence of rutile and the notable absence of ilmenite as inclusions in garnet (Figs 5f & S1). Similar observations from the more typical Sil + Ky-bearing felsic granulite samples

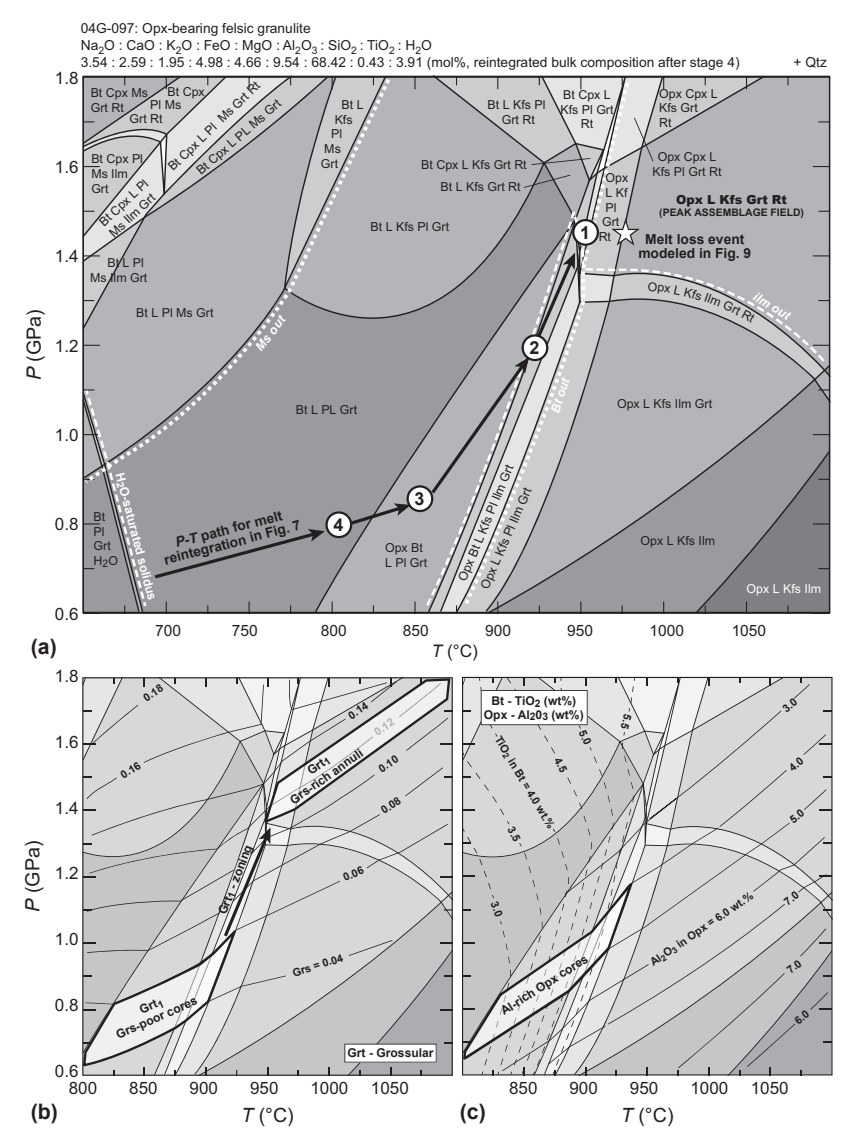


Fig. 8. (a) P-T pseudosection derived with Perple X 6.6.8 using the reintegrated bulk composition for 04G-097 after the fourstage melt reintegration procedure (Fig. 7; Table S4). The black arrow corresponds to the inferred P-T path along which the melt reintegration was performed. The numbers denote the P-T conditions for each stage of the modelled melt reintegration. Note the peak assemblage for sample 04G-097 at upper right: Opx + Grt + Rt + Ternary Feldspar + Melt. Boundaries for Ms-out, Bt-out, Ilm-out and the H₂O-saturated solidus are highlighted with dashed lines. Location of the melt loss event modelled in Fig. 9 is denoted by the star. (b) High-Tside of same P-T pseudosection in (a) with isopleths for mole fraction of grossular in garnet. Note the highlighted fields corresponding to the measured compositions of Grt1 cores and annuli and the P-T path between them inferred from grossular zoning. (c) Same P-T pseudosection as in (b) with isopleths for wt% TiO₂ in biotite and wt% Al₂O₃ in orthopyroxene. Note the highlighted field corresponding to core compositions measured in Opx for 04G-097.

support reducing conditions $(X_{\text{Fe}_2\text{O}_3} \ll 0.05; \text{Fig. S6b})$, including the absence of ilmenite and the presence of graphite as inclusions in garnet and throughout the matrix (Fig. S2).

Orthopyroxene-bearing felsic granulite 04G-097: melt reintegration and constraints on prograde evolution and peak metamorphism

The Opx-bearing felsic granulite (04G-097) preserves evidence for a prograde evolution involving the production of Al-rich Opx and grossular-poor garnet cores that transition into grossular-rich garnet annuli associated with Ti-rich biotite inclusions and polyphase inclusions of Kfs + Pl + Qtz + Bt + Rt. Because this rock was affected by melt loss, the down-temperature melt reintegration approach of Korhonen *et al.* (2013) was applied to reconstruct a plausible protolith bulk composition to model the prograde phase relations.

The first stage of melt integration was performed in the stability field where the peak metamorphic assemblage $(Opx + L + Kfs \pm Pl + Grt + Rt + Qtz)$ was observed at >1.4 GPa and >925 °C (Fig. 7). The precise P-T location of the melt integration step is not critical as the melt composition does not vary significantly within this stability field (cf. Korhonen et al., 2013). We selected a point located on the 1 mol.% melt isopleth at a pressure of 1.45 GPa (Fig. 7), corresponding to the amount of melt that would be retained as thin films along grain boundaries after melt loss (Yakymchuk & Brown, 2014a). At this point, 6 mol.% melt was added to the bulk composition to reach a value of 7 mol.% melt in the rock. This volume of melt is analogous to the maximum threshold for melt interconnection and transfer based on experimentally constrained observations of the melt connectivity transition (Rosenberg & Handy, 2005). The new bulk composition obtained after melt reintegration was used to compute a new pseudosection

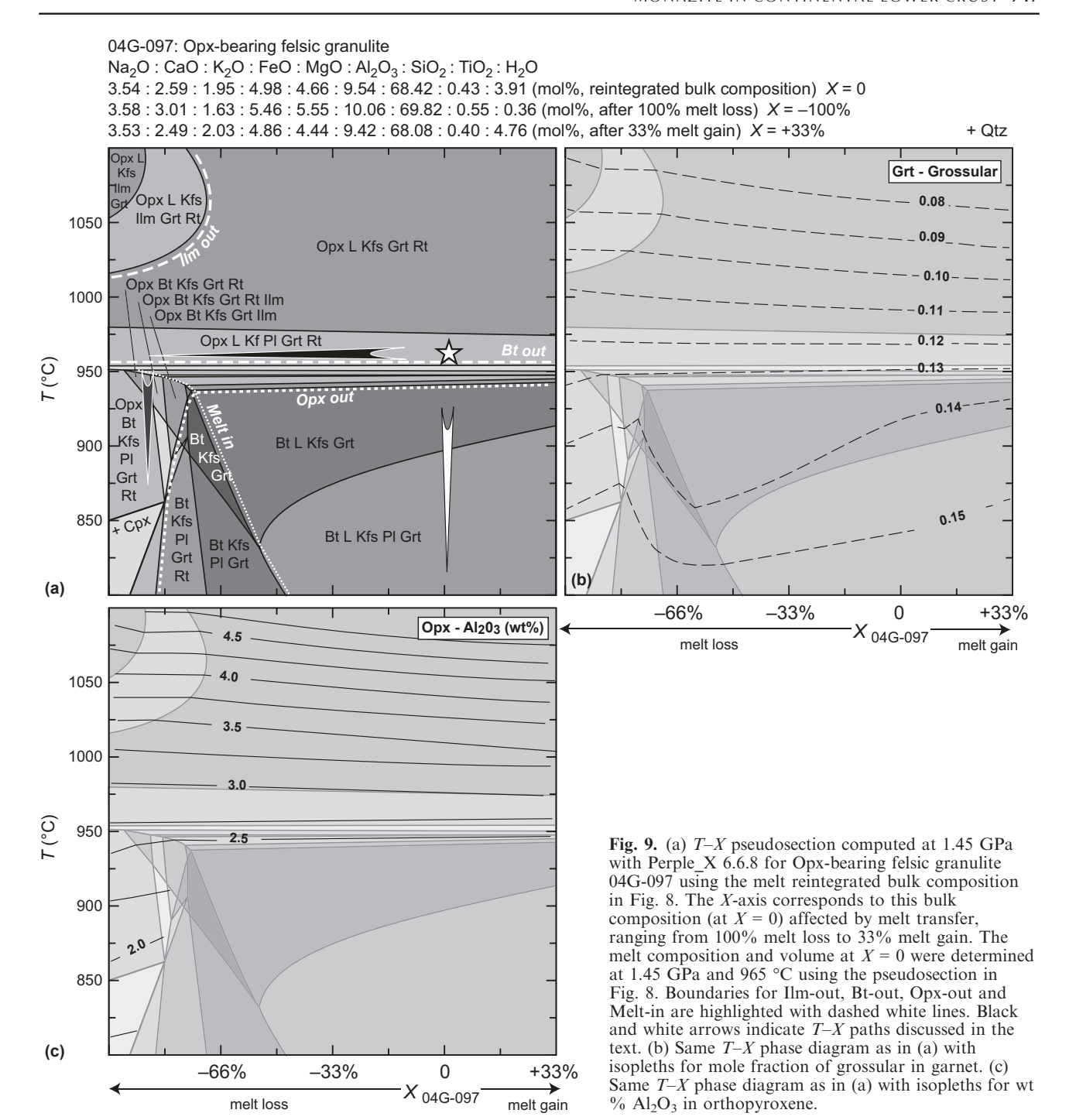


(Fig. 7; Table S4). Down-temperature melt reintegration was carried out along an inferred prograde P–T path corresponding to the burial of sediments to a depth in excess of 50 km (>1.4 GPa; P–T path in Figs 7 & 8). The low-P portion of the path represents burial of the sediments from the surface to 850 °C and 0.85 GPa. For >850 °C, it is assumed that the temperature during burial to > 1.4 GPa was buffered by the fluid-absent biotite melting reaction. Subsequent melt

reintegration steps were defined where the P-T path crossed the 1 mol.% melt isopleth (Fig. 7).

Four melt reintegration steps, representing addition of \sim 25 mol.% melt, were necessary to produce a plausible protolith bulk composition such that the solidus was H₂O-saturated (Fig. 8). The primary effect of adding melt to the initial residual bulk composition was the addition of H₂O (Table S4). The main features of the pseudosection computed with

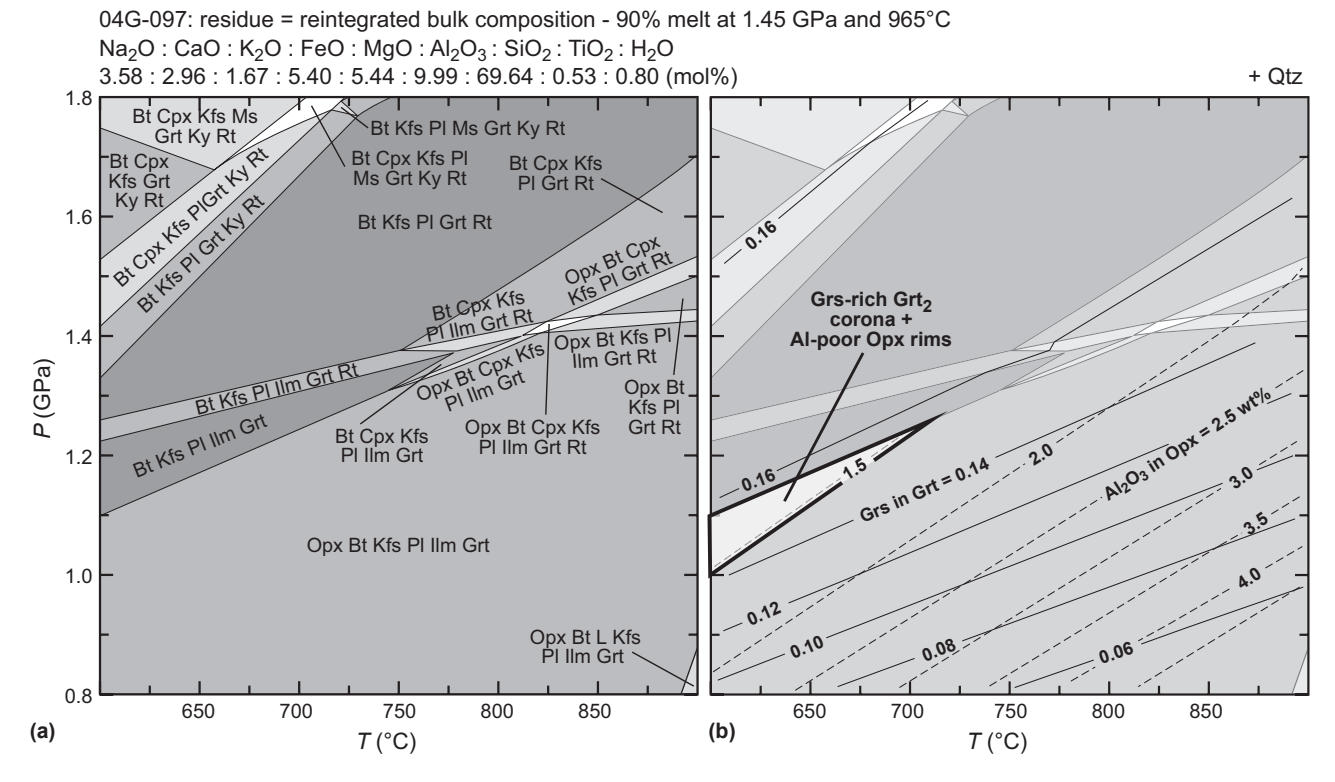


Fig. 10. (a) *P*–*T* pseudosection derived with Perple_X 6.6.8 for residual Opx-bearing felsic granulite bulk composition for sample 04G-097 (in Fig. 8) after 90% melt loss at 1.45 GPa and 965 °C. (b) Same *P*–*T* phase diagram as in (a) with isopleths for mole fraction of grossular in garnet and wt% Al₂O₃ in orthopyroxene. Note highlighted melt-absent field defining compositions for high-grossular Grt₂ and recrystallized low-Al Opx measured in 04G-097.

the derived protolith composition are consistent with constraints from partial melting experiments using a greywacke bulk composition (Fig. 8; Vielzeuf & Schmidt, 2001). These features include: (i) a water-saturated solidus at 650–675 °C, (ii) the fluid-absent muscovite melting reaction at >1.0 GPa between 700 and 800 °C (Ms-out in Fig. 8a), (iii) a large *P-T* region between 700 and 875–950 °C where the incongruent biotite melting reaction produces peritectic garnet + melt and (iv) a steep and narrow low-variance field between 875 and 950 °C corresponding to the fluid-absent biotite melting reaction and the production of peritectic Opx + Kfs + Grt (Fig. 8a).

The high-*T* side of the pseudosection derived from the melt reintegrated bulk composition was contoured for mole fraction of grossular in garnet (Fig. 8b), wt% TiO₂ in biotite and wt% Al₂O₃ in orthopyroxene (Fig. 8c). Grossular-poor garnet cores (Grs₃₋₄) reported for Grt₁ are most compatible with low-*P* growth at 0.6–0.8 GPa and 800–900 °C (Fig. 8b). This garnet composition would be in equilibrium with aluminous orthopyroxene (4.5–6 wt% Al₂O₃; Fig. 8c), consistent with the core compositions measured in orthopyroxene porphyroblasts (up to 4.48 wt% Al₂O₃; Table S2). The low-grossular cores of Grt₁ porphyroblasts are surrounded by grossular-rich annuli (up to Grs₁₃) that contain Ti-rich biotite (6.07 wt% TiO₂) and poly-phase inclusions of Bt +

Pl + Qtz + Kfs + Rt (Fig. 5f), interpreted as relicts of crystallized melt. The garnet zoning and textures are most consistent with a loading path from 0.6-0.8 to >1.4 GPa. This path was likely buffered in temperature by the low-variance fluid-absent biotite melting reaction and crossed the grossular isopleths at a relatively high angle before reaching the peak assemblage stability field of Opx + L + Kfs + Grt + Rt at UHT (Fig. 8a,b). The inferred loading path in Fig. 8b coincides with increasing vol.% garnet, modest amounts of melt production (~25 vol.%) and a diminishing abundance of ilmenite, consistent with petrographic observations. Measured and modelled Ti contents up to 6.25 wt% TiO2 in resorbed biotite inclusions in garnet and ternary feldspar are consistent with prograde partial melting of biotite at temperatures in excess of 900 °C (Fig. 8c). The presence of rutile is critical for constraining a minimum pressure of ~1.3 GPa at >950 °C (above 'Ilm-out' in Fig. 8a). Peak metamorphic conditions were refined by using the maximum measured grossular content of the Grt_1 annuli (up to $12 \pm 1\%$) in equilibrium with orthopyroxene and rutile, corresponding to 1.35-1.8 GPa and 950-1100 °C (Fig. 8b, c). At these peak conditions, the Al₂O₃ content of orthopyroxene would decrease to ~3 wt% Al₂O₃ (Fig. 8c), consistent with the observed core-to-rim zoning (Fig. 5c).

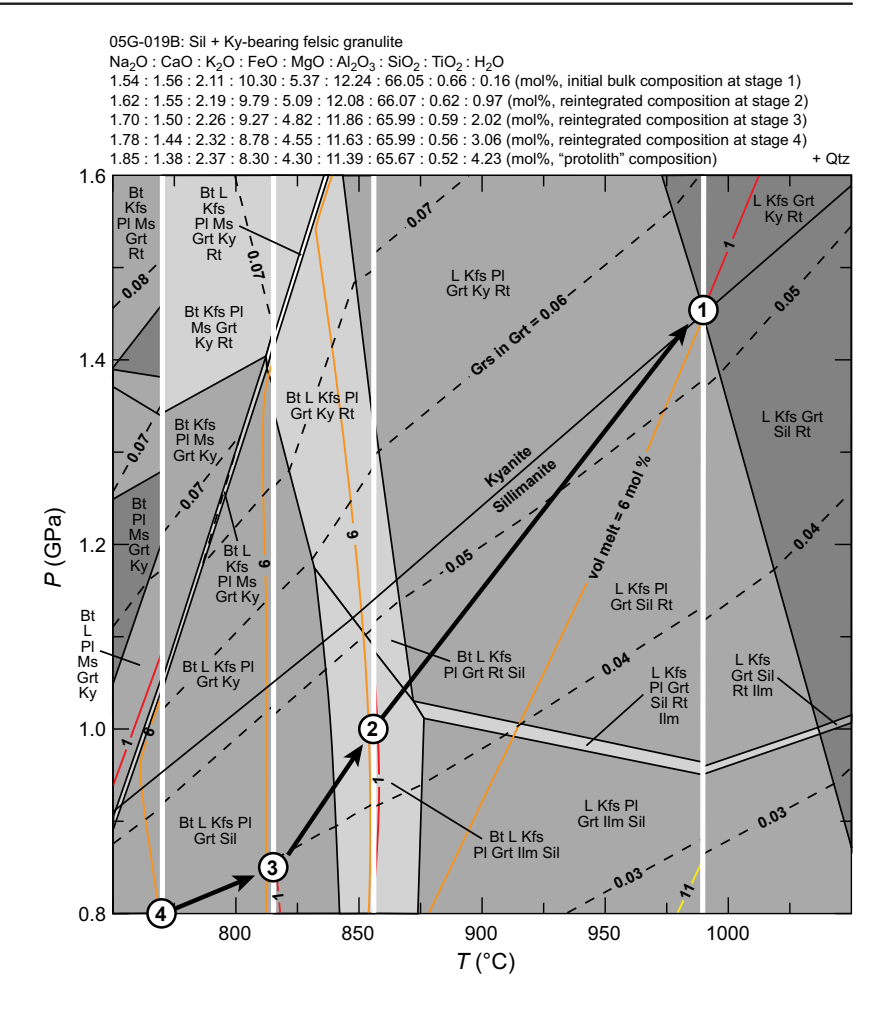


Fig. 11. (a) Melt reintegration model represented as a composite pseudosection computed with Perple_X 6.6.8 for Sil + Kybearing felsic granulite 05G-019B. Coloured contours correspond to mol.% melt isopleths. Dashed black lines represent isopleths for mole fraction of grossular in garnet. The far right panel corresponds to the P-T pseudosection calculated for the starting residual whole-rock bulk composition in Table S1 + 0.04 wt% H₂O to achieve ~1 mol.% melt at the inferred peak conditions. The four adjacent panels illustrate the effect of melt reintegration into the residual bulk composition such that a melt connectivity threshold of 7 mol.% melt (~7 vol.%) was reached at each stage. Four melt reintegration stages (numbers 1-4) were performed at the 1 mol.% melt isopleth down pressure and temperature along a hypothetical P-T path similar to the path imposed for sample 04G-097 in Figs 7 and 8. The composition of melt and the reintegrated bulk composition for each stage are provided in Table S4.

We infer that partial melting and the formation of Opx + Grt₁ occurred during a loading path from 0.6-0.8 to >1.35 GPa at a temperature that was buffered by the fluid-absent biotite melting reaction at ~900–950 °C. The pseudosection in Fig. 8 that facilitates this inference is based on the assumption that the entire prograde evolution occurred under a closed system. In the following section, we explore the effect of melt transfer at peak metamorphic conditions.

Orthopyroxene-bearing felsic granulite 04G-097: effect of melt transfer

The development of grossular-rich (up to Grs₁₆) coronitic Grt₂ around low-Al dynamically recrystallized orthopyroxene (1.08 wt% Al₂O₃) cannot be explained by the pseudosection in Fig. 8. Although the Grs_{16} isopleth in Fig. 8c occurs at P-T conditions of >1.4 GPa and 800-925 °C, it is noteworthy that this garnet composition would be in equilibrium with a melt-bearing assemblage that does not contain stable orthopyroxene. To reconcile observations with the predicted phase relations, we carried out several models to constrain the effect of melt transfer.

Figure 9 is a T-X pseudosection calculated at 1.45 GPa. The X-axis corresponds to the melt reintegrated bulk composition of 04G-097 affected by a range of melt transfer from 100% melt loss to 33% melt gain. The starting melt composition and volume at X = 0 were determined at 1.45 GPa and 965 °C using the pseudosection in Fig. 8. These P-T conditions are located just above the completion of the fluid-absent biotite melting reaction (star in Fig. 8a). At peak metamorphic conditions above 950 °C, melt transfer has no significant effect on phase relations (Opx + L + Kfs + Grt + Qtz field in Fig. 9a) or mineral composition (Fig. 9b,c). The most prominent effect of melt loss is visible at temperatures lower than 950 °C. If isobaric cooling occurred under closed system conditions (white arrow in Fig. 9a), orthopyroxene would become unstable in the presence of melt. In contrast, significant melt loss (90% or more) followed by an episode of isobaric cooling (black arrows in Fig. 9a) would stabilize low-Al orthopyroxene at sub-solidus conditions (Fig. 9c).

Figure 10 corresponds to a P-T pseudosection calculated with the residual bulk composition obtained after a loss of 90% of the melt produced at 1.45 GPa and 965 °C. The main effect of melt loss is to stabilize low-Al orthopyroxene in equilibrium with highgrossular garnet at sub-solidus conditions (Figs 9a & 10). Another notable effect of melt loss is the stabilization of ilmenite to lower temperatures (cf. Figs 8a & 10a). Although rutile is the main Ti-bearing phase at peak metamorphic conditions based on the abundant occurrence of rutile inclusions in Grt₁ (Fig. 5f), ilmenite is an abundant matrix phase that has been observed in contact with rutile in the vicinity of coronitic Grt₂ which, in turn, surrounds orthopyroxene and Grt₁ (Fig. 5a). Mineral composition contours suggest maximum P-T conditions for the formation of low-Al orthopyroxene and coronitic Grt₂ in association with ilmenite at 600-675 °C and 1.0–1.2 GPa (highlighted field in Fig. 10b).

Sillimanite + kyanite-bearing felsic granulite 05G-019B: *P-T* conditions

Precise thermobarometric constraints from the more widespread aluminosilicate-bearing felsic granulite gneisses in the Upper Deck domain are limited by their high-variance mineral assemblages (Sil \pm Ky +Kfs + Grt + Rt + Qtz). Textural observations support equilibrium of ternary feldspar with kyanite, an inference that requires minimum P-T conditions of ~1.5 GPa and 950 °C (Snoeyenbos et al., 1995). We explored the plausibility of these conditions along a prograde loading P-T path similar to that inferred previously and modelled for the orthopyroxene-bearing felsic granulite (Fig. 11). The residual bulk composition for 05G-019B was used for the first stage of the melt reintegration (Fig. 11; Table S4). The initial H_2O content was adjusted (0.04 wt% $\approx 0.16 \text{ mol.}\%$) to ensure that 1 mol.% melt was present at the inferred peak conditions, representing what would have been melt films retained after melt loss. Subsequent melt reintegration steps along the P-T path in Fig. 11 involved the addition of 6 mol.% melt to the bulk composition and recalculation of a new pseudosection, as discussed previously for sample 04G-097. Each pseudosection was contoured with isopleths for mol.% melt and mole fraction of grossular in garnet (Fig. 11).

The composite P-T pseudosection modelled with the kyanite-bearing felsic granulite bulk composition reveals two large stability fields at >1.0 GPa and >850 °C where melt is in equilibrium with Kfs \pm Pl + Grt + Ky (or Sil) + Rt (Fig. 11). The low-T and low-P boundaries of these stability fields correspond to the appearance of biotite and ilmenite respectively (Fig. 11). The continuous change in high-phosphorous garnet composition (Grt₁) from a low-grossular core (Grs₃₋₄) to a high-grossular annulus (Grs₇₋₁₁) and the garnet core-to-rim transition from sillimanite inclusions to kyanite inclusions (Fig. 6a) are consistent with the inferred loading path illustrated in Fig. 11. The peak assemblage of high-grossular Grt₁

annuli in equilibrium with L + Kfs + Ky + Rt would have been stable at >1.4 GPa and >975 °C (Fig. 11), consistent with the original conclusions of Snoeyenbos *et al.* (1995).

The second-generation low-phosphorous garnet rim (Grt_2 in Fig. 6) is characterized by a low-grossular composition (Grs_{3-5}) intergrown with retrograde plagioclase (Fig. 6a,b). The stability of low-grossular garnet + plagioclase in the absence of melt is largely outside the range of P-T conditions modelled in Fig. 11. We suggest that Grt_2 may have grown in equilibrium with plagioclase as a sub-solidus assemblage during a period of reheating after cooling to an ambient crustal geotherm. A different effective bulk composition would be required to accurately model the conditions for growth of Grt_2 .

MONAZITE TRACE ELEMENT ANALYSIS AND GEOCHRONOLOGY BY EPMA

procedure for Th-U-total Pb monazite geochronology and trace element analysis by EPMA in this study follows the work of Jercinovic & Williams (2005), Williams et al. (2006, 2007), Jercinovic et al. (2008) and Dumond et al. (2008). Calibrated overlap correction factors for peak interferences of $YL\gamma$ on $PbM\alpha$, $ThM\zeta 1$ and $ThM\zeta 2$ on $PbM\alpha$, second-order LaL α on PbM α , ThM γ on UM β , KK α on $Um\beta$, and $NdL\beta 3$ on $EuL\alpha$ were applied prior to ZAF corrections during the analytical sessions (see Donovan et al., 1993; Pyle et al., 2002, 2005; Jercinovic & Williams, 2005; Jercinovic et al., 2008). Full thin-section X-ray maps were collected via EPMA to identify all monazite grains (e.g. Fig. S3; following Williams & Jercinovic, 2012). Monazite grains were mapped at high spatial resolution (0.3–0.5 μ m step sizes) at 15 kV and 200 nA for 70–100 ms per pixel on a Cameca[®] SX50 electron microprobe. X-ray maps for $YL\alpha$, $CaK\alpha$, $ThM\alpha$ and $UM\beta$ were processed both simultaneously and then, individually to identify similar and compositionally distinct domains to guide subsequent quantitative analysis. Details regarding the analytical methods for monazite trace element analysis by EPMA and the determination of each domain-specific date and error are summarized in Williams et al. (2006) and Dumond et al. (2008). All dates are plotted as histograms scaled relative to a consistency standard (Williams et al., 2006). The standard used in this study is the Moacir Brazilian pegmatite monazite with a weighted mean 207Pb/235U age of 504.3 \pm 0.2 Ma (2 σ , MSWD = 0.64) (Gasquet et al., 2010).

Twenty-nine compositional domains were analysed in monazite grains in samples 04G-097, 05G-019B and 05G-026B using the Cameca[®] SX100 Ultrachron electron microprobe at the University of Massachusetts-Amherst. The span of ages from 2.66 to 1.89 Ga is similar to that identified by Baldwin *et al.* (2006). The data set consists of matrix grains, inclusions in garnet

and intergrowths with garnet rims (Table S5). Textural observations were combined with major and trace element data for each monazite domain to link monazite to episodes of partial melting, garnet growth and feldspar recrystallization (see Discussion).

Monazite compositional zoning and textural setting

Four distinct compositional domains are present in monazite grains from all felsic granulite samples. Domain 1 monazite consists of rare resorbed high-Y cores (Figs 12a & 13a-c). Domain 2 monazite, which consistently occurs as overgrowths around domain 1 cores and locally contains inclusions of K-feldspar (Figs 12a & 13c), is defined by high-Th, high-Ca and low-Y (Figs 12a & 13c) and includes cores of grains with oscillatory or sector zoning defined by Th (Fig. 13d). Domain 3 monazite is defined by low-Th. low-Ca rims on domain 2 monazite (Figs 12a,b & 13d,e). Monazite domains 2 and 3 have each been observed at least once in the high-grossular annulus of Grt₁ (Figs 12b & 13e). Domain 4 monazite predominantly occurs as thin rims (10 μ m-wide or less) that are slightly enriched in Th + Ca relative to domain 3 monazite (Figs 12c,d & 13f). Less commonly, domain 4 occurs as rims on monazite inclusions in the fractured rims of low-phosphorous Grt₂ in sample 05G-019B (Fig. 13f) and as intergrowths with Grt₂ (Fig. 13g). More commonly, domain 4 monazite occurs as outermost rims on matrix grains (Figs 12c.d. 13h & 14b) which are associated with recrystallized ribbons and grains of ternary feldspar (Figs 12d, 13h & 14a). Thorium zoning in domain 4 rims of matrix monazite locally defines asymmetric overgrowths consistent with dextral, top-to-the-NE oblique-slip displacement in Opx-bearing felsic granulite (sample 04G-097; Fig. 12d) and elongate syntectonic overgrowths in D₂ dextral ultramylonite zones (sample 05G-026B; Figs 14b & S3).

Monazite geochemistry and geochronology

Geochemical data and calculated Th–U–total Pb dates are summarized in Figs S7 and S8 and Table S5. Many of the dates yield 2σ uncertainties in the order of ± 18 –55 Ma. Large errors (in excess of ± 60 Ma) for some monazite domains discussed below are attributed to low-Th concentrations (≤ 0.78 wt% ThO₂ in Table S5). Most domains display a positive Eu-anomaly (Eu* = 1.5–18.9) in contrast to nearly all published data which depict negative Eu-anomalies in monazite (Fig. S7; Table S5; see Discussion; Bea, 1996; Bea & Montero, 1999; Hermann & Rubatto, 2003; Kelly et al., 2006; Rubatto et al., 2006). All monazite domains, with the exception of domain 1, are low in Y (< 800 ppm Y; Table S5).

The high-Y $(1.46-1.84 \text{ wt}\% \text{ Y}_2\text{O}_3)$ domain 1 monazite cores were dated at 2636 \pm 20 to 2615 \pm 21 Ma $(2\sigma; \text{Figs } 12a \& 13a,b; \text{Table S5})$. Dates for domain 2

monazite cores and overgrowths range from 2613 ± 18 to 2552 ± 19 Ma (2σ) with a marked enrichment in Th (4.79-20.00 wt% ThO₂) and depletion in Y (<800 ppm) relative to domain 1 (Figs 12a & 13c,d; Table S5). Domain 3 low-Th monazite rims (0.05-6.20 wt% ThO2) tend to yield dates with large uncertainties ranging from 2664 ± 247 to 2514 ± 47 Ma (2σ) ; Figs 12a,b, 13d,e & 14b; Table S5). Domain 3 monazite rims are also distinctly depleted in Ca (0.07-0.91 wt% CaO) and Sm (below detection – 0.92 wt% Sm₂O₃) with respect to domains 2 and 3 (Table S5). Four of the analysed grains with domain 3 rims are completely included in the highgrossular annulus of Grt₁ (Figs 5e, 12a,b & 13e; grains 05G-019B-YZ-1-m18 and 05G-019B-YZ-2-m9 in Table S5). Comparison of domain 2 core and domain 3 rim data for three of the monazite grains reveals marked enrichments in $X_{\text{LaPO}_4} + X_{\text{CePO}_4}$ and X_{EuPO_4} from core to rim (arrows in Fig. S8a,b). The four domain 3 monazite rims in sample 05G-019B have some of the largest Eu-anomalies in the entire data set (7.6–14.4) and together yield a weighted mean age of 2539 ± 21 Ma $(2\sigma, MSWD = 3)$ for growth of Euenriched, Th- and Ca-depleted monazite (Fig. S8c; Table S5). The relatively large MSWD may indicate a period of protracted monazite growth, instead of a single discrete event. Domain 4 monazite grains are highly depleted in Th (0.07-1.41 wt% ThO₂) and are generally the most enriched in La + Ce (Fig. S8a; Table S5). Dates for domain 4 monazite range between 2020 ± 355 and 1885 ± 20 Ma (2σ : Figs 12c.d. 13f-h & 14b; Table S5). Five dates for domain 4 matrix monazite grains and monazite cores or rims included in or intergrown with Grt2 rims (Fig. 13f,g) yield a weighted mean age of $1913 \pm 25 \text{ Ma}$ MSWD = 0.1) for growth of domain 4 monazite (Fig. S8c). Three dates for elongated overgrowths of domain 4 monazite in the 05G-026B ultramylonite provide a weighted mean age of 1924 \pm 72 Ma (2 σ , MSWD = 0.2) for growth of domain 4 monazite (Figs 14b & S8c; Table S5). Three dates for syn-kinematic dextral overgrowths in the 04G-097 Opx-felsic granulite yield a weighted mean age of 1897 \pm 11 Ma $(2\sigma, MSWD = 2)$ for dextral shearing and growth of domain 4 monazite (Figs 12c,d & S8c; Table S5).

DISCUSSION

Phase equilibria modelling and melt reintegration techniques applied to residual peraluminous bulk compositions is consistent with fluid-absent biotite melting and peritectic garnet growth along a prograde loading path from ≤ 0.8 to ≥ 1.4 GPa, culminating with UHT conditions (>950 °C; Figs 8 & 11). These results are in agreement with previous P-T estimates determined for the felsic granulite gneisses (Snoeyenbos *et al.*, 1995) and for mafic granulite gneisses interlayered with the felsic gneisses (Snoeyenbos *et al.*, 1995; Baldwin *et al.*, 2003). Melt must

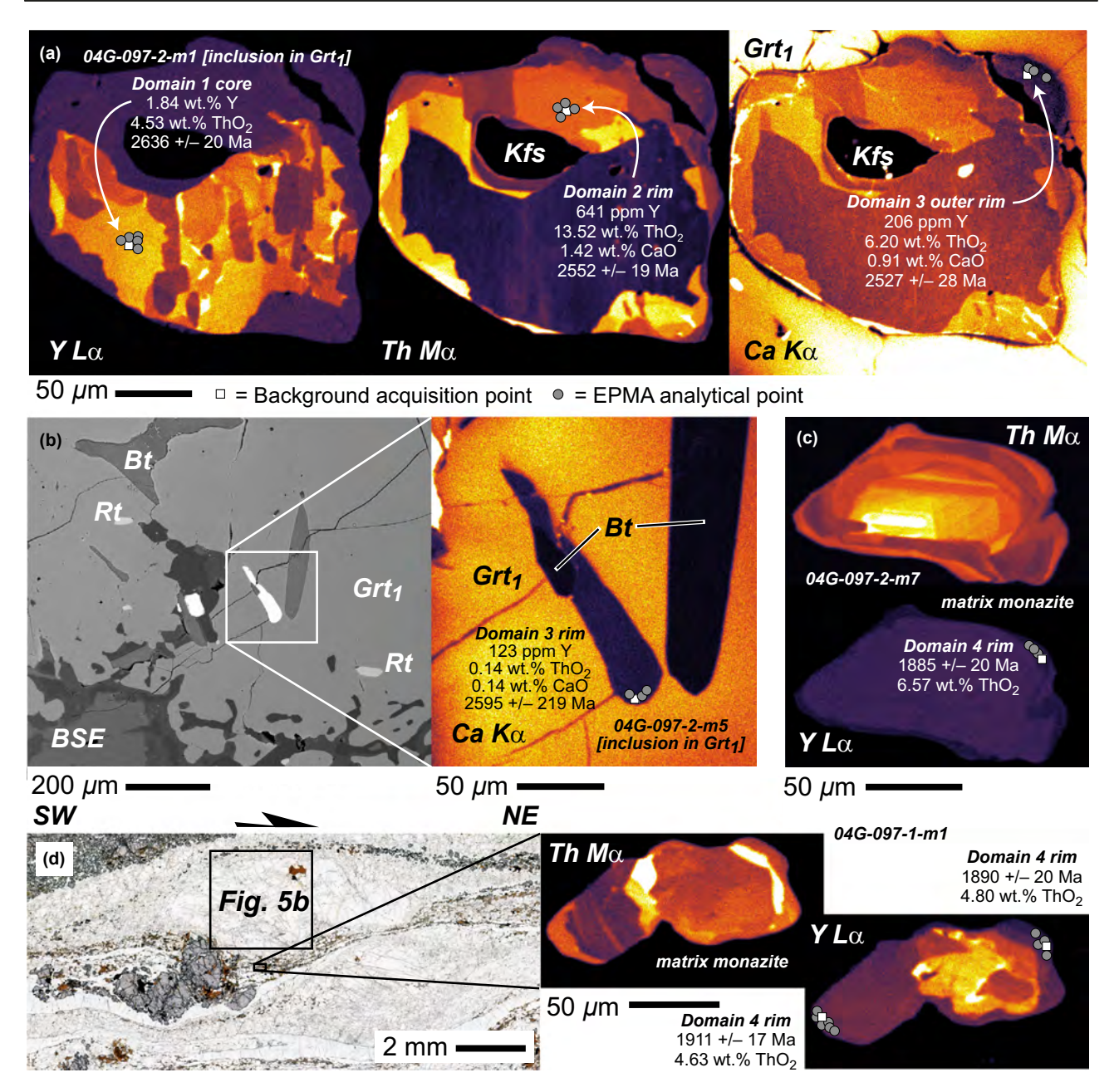


Fig. 12. Monazite maps and data for Opx-bearing sample 04G-097. Grains in (a) and (b) are inclusions in the high-grossular annulus of Grt_1 . Grains in (c) and (d) occur in the matrix. (a) X-ray maps of monazite grain 2 m1 with EPMA Th–U–total Pb dates $(\pm 2\sigma)$. (b) Backscattered electron (BSE) image of textural setting of monazite grain 2-m5 in garnet with X-ray map depicting EPMA Th–U–total Pb date $(\pm 2\sigma)$. (c) X-ray maps of monazite grain 2-m7 with EPMA Th–U–total Pb date $(\pm 2\sigma)$. (d) Plane polarized light photomicrograph illustrating setting of monazite grain 1-m1 beneath a large dextral ternary feldspar σ -clast. Note syn-kinematic rims on 1-m1 depicted in the Th $M\alpha$ map and EPMA Th–U–total Pb dates $(\pm 2\sigma)$ on rims in the YL α map.

have been lost from these residual felsic granulites to facilitate preservation of peak metamorphic assemblages (Brown, 2002; White & Powell, 2002; White *et al.*, 2004). These results provide context for understanding the petrogenesis of monazite in continental lower crust.

Compositional zoning defined by X-ray maps, in combination with major and trace element data, pro-

vide a basis for inferring monazite petrogenesis with respect to prograde and retrograde silicate reactions (see review by Williams *et al.*, 2007). What remains less well-understood, however, is the behaviour of Y, Th and other elements in monazite during partial melting or melt extraction (Watt & Harley, 1993; Watt, 1995; Kohn *et al.*, 2005). Establishing links between growth/dissolution/re-precipitation of monazite and

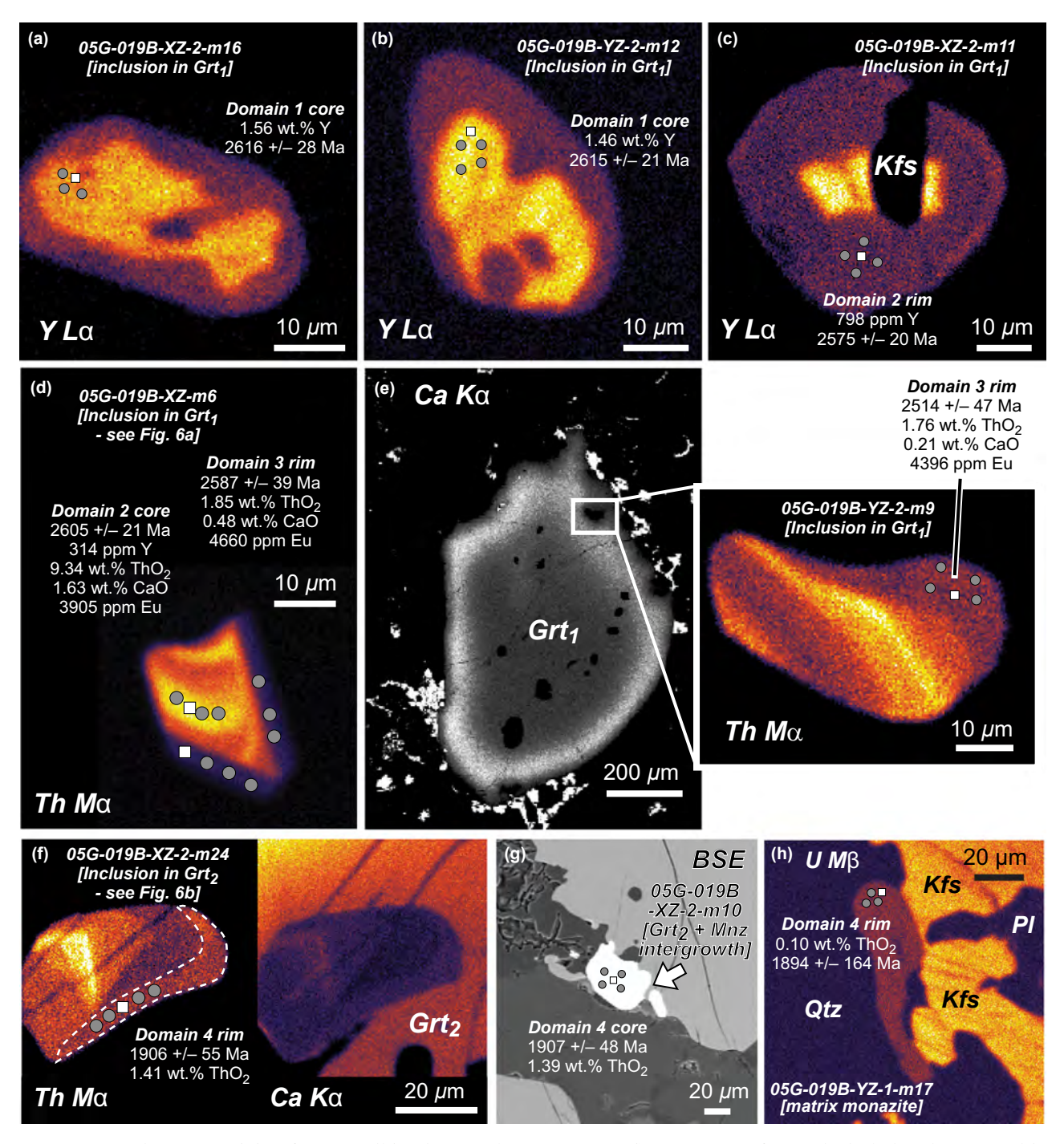
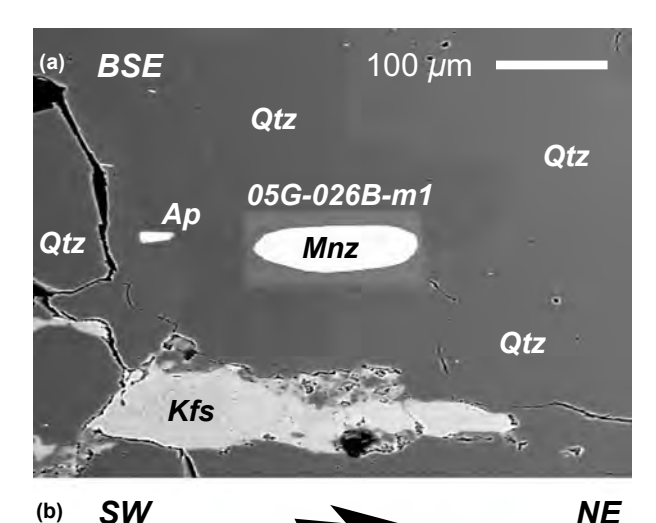
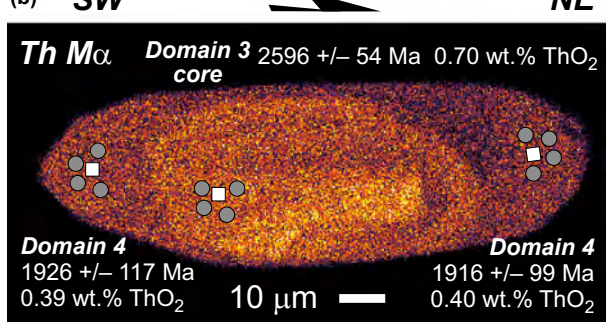


Fig. 13. Monazite maps and data for Ky + Sil-bearing sample 05G-019B. (a–d) X-ray maps of monazite inclusions in garnet with EPMA Th–U–total Pb dates $(\pm 2\sigma)$. (e) Ca $K\alpha$ map of garnet depicting location of monazite grain YZ-2-m9 in high-grossular annulus of Grt₁ with EPMA Th–U–total Pb date $(\pm 2\sigma)$. (f) X-ray maps of monazite grain XZ-m24 included in Grt₂ rim with EPMA Th–U–total Pb date $(\pm 2\sigma)$. (g) Backscattered electron image of monazite intergrowth with Grt₂ rim with location of EPMA Th–U–total Pb date $(\pm 2\sigma)$. (h) X-ray map of matrix monazite grain with EPMA Th–U–total Pb date $(\pm 2\sigma)$.

the appearance or loss of melt or a major silicate phase requires knowledge of REE-residence in the various phases (Bea, 1996; Jung & Hellebrand, 2006). Our results combined with existing data on REE abun-

dance in crustal granulites are used to constrain a model for the role of monazite as a monitor of partial melting, garnet growth and feldspar recrystallization in continental lower crust (Fig. 15).





- □ = Background acquisition point
- = EPMA analytical point

Fig. 14. Monazite maps and data for felsic granulite ultramylonite sample 05G-026B. (a) High-contrast backscattered electron (BSE) image of textural setting of elongate monazite in the large recrystallized quartz ribbon illustrated in Fig. S3. (b) Th $M\alpha$ map of same monazite grain with EPMA Th–U–total Pb dates $(\pm 2\sigma)$.

Monazite as a monitor of garnet growth and melting

Monazite exhibits strong depletions in Y + HREEs when it precipitates during or after the growth of garnet, a phase that readily incorporates Y + HREEs (Bea & Montero, 1999; Zhu & O'Nions, 1999a). Numerous workers have used Y-zoning in monazite to infer the relative timing of garnet growth when no other Y-bearing phases are present in the assemblage (Zhu & O'Nions, 1999b; Foster et al., 2002, 2004; Pyle & Spear, 2003; Gibson et al., 2004; Kohn et al., 2005; Kelly et al., 2006; Mahan et al., 2006a; Dumond et al., 2010). Texturally resorbed high-Y domain 1 monazite cores identified in both orthopyroxene-bearing (sample 04G-097) and kyanite-bearing felsic granulites (sample 05G-019B) are inferred to represent relicts of detrital monazite grains that existed prior to peritectic garnet growth in the felsic granulites (Figs 12a & 13a-c). We suggest that the resorption of domain 1 monazite marks the onset of melting and the incorporation of Y liberated by dissolution of monazite into peritectic garnet (stage 2 in Fig. 15). Domain 2 monazite cores and overgrowths are depleted in Y and enriched in Th and Ca relative to domain 1. Monazite and garnet are the only Y-bearing phases in the felsic granulite gneisses, and thus the depletion of Y observed in domain 2 implies growth of monazite during or following the appearance of garnet. The occurrence of Y-depleted domain 2 monazite as inclusions in Grt₁ in samples 04G-097 and 05G-019B supports a syn-garnet interpretation for monazite growth between 2.61 and 2.55 Ga (stage 3 in Fig. 15). Ca-enrichment in domain 2 monazite may be due to breakdown of plagioclase during melting and/or dissolution of apatite.

The dramatic enrichment in Th is interpreted in the context of two fluid-absent melting reactions (Fig. 15). For the orthopyroxene-bearing felsic granulite, the results support a reaction of the type Bt + $Pl + Qtz + high-Y, low-Th Mnz \rightarrow Grt + Opx + Kfs$ + Melt + low-Y, high-Th Mnz. For the aluminosilicate-bearing felsic granulite, the results support a reaction of the type Bt + Pl + Sil + Qtz + high-Y, low-Th Mnz → Grt + Kfs + Melt + low-Y, high-Th Mnz. Preferential incorporation of Th and loss of Y in domain 2 monazite is most consistent with growth of monazite in the presence of melt + garnet \pm K-feldspar. This is supported by the occurrence of K-feldspar inclusions (inferred to represent products of the melting reaction) that cut across domain 1 and are overgrown by domain 2 monazite in both types of felsic granulite (Figs 12a & 13c).

Incorporation of Th into monazite in the presence of melt requires the partition coefficient for Th between monazite and melt to be greater than 1 (Rapp et al., 1987), as recently demonstrated experimentally by Xing et al. (2013) for monazite in haplogranite melts. Evidence for compatible behaviour between Th and monazite is implied by high-Th oscillatory-zoned grains that arguably crystallized in the presence of melt (e.g. core of grain 05G-019B-XZ-m6 in Fig. 13d). Thus, domain 2 is regarded as a direct record of melting and peritectic garnet growth such that Y from monazite was incorporated into garnet and Th from the melt was incorporated into monazite during prograde melting (stage 3 in Fig. 15). Because S₁ fabrics in the Upper Deck domain are defined by the products of partial melting, e.g. residual garnetite layers and leucosomes (Figs 3a-d & 4a,b), the c. 2.61-2.55 Ga dates for domain 2 broadly constrain the age of the S₁ fabric and concomitant melt-weakened lower crustal flow. This interpretation indicates a Neoarchean age for Grt₁ in all samples, as concluded for granulites in the Northwestern (Fig. 1; Dumond et al., 2010; Regan et al., 2014) and Chipman domains (Flowers et al., 2008; Mahan et al., 2008).

Monazite as a monitor of melt extraction

Melt extraction has been inferred from our field observations and phase relationships. Experimental

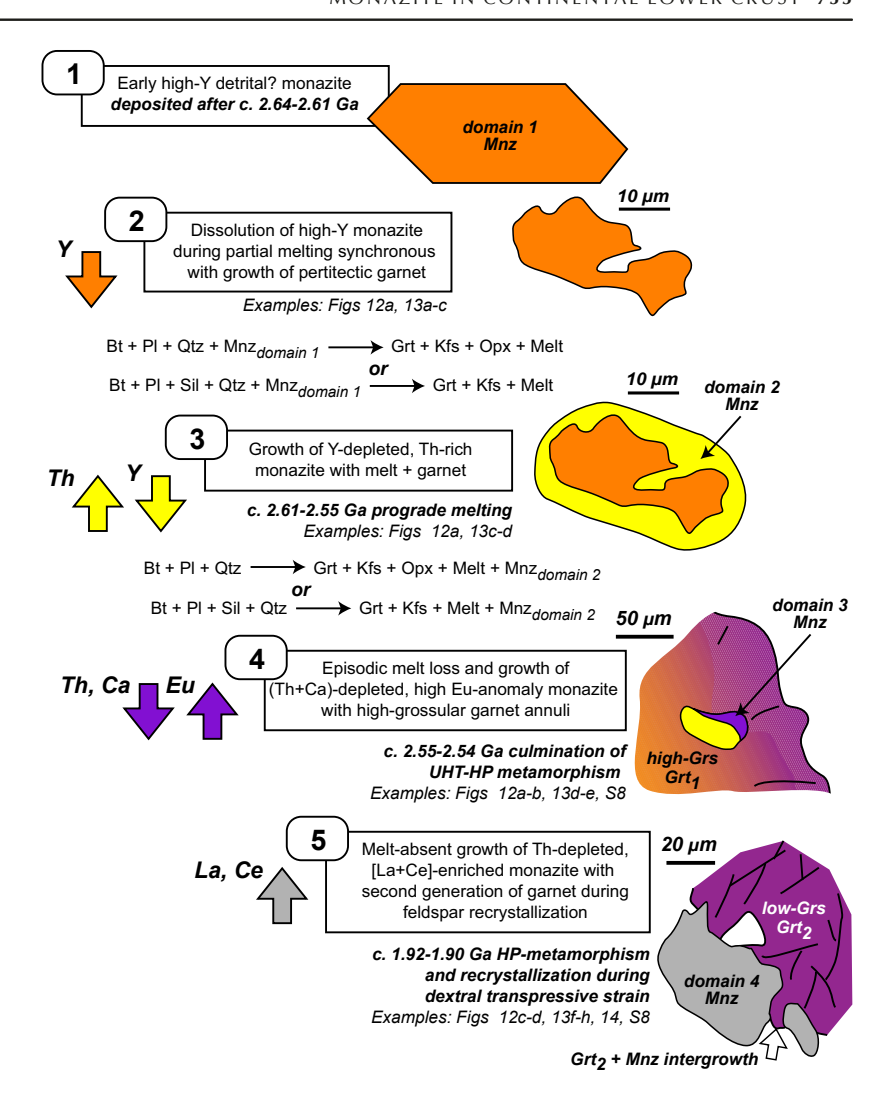


Fig. 15. Five-stage model for monazite behaviour during melting, garnet growth and feldspar recrystallization in continental lower crust based on this study. Colours for monazite domains are the same as in Fig. S8. See text for discussion.

work has demonstrated that Th partitions preferentially into haplogranite melts rather than into the solid residues (Keppler & Wyllie, 1990), but also that Th partitions preferentially into monazite in relation to melt (Xing et al., 2013). Consequently, melt extraction during partial melting may leave behind a residue that is progressively depleted in Th, and retention of monazite during melting or fractional crystallization of monazite from melt will also leave the melt depleted in Th. The sharp drop in Th that marks the boundary between high-Th domain 2 cores and low-Th domain 3 rims in monazite denotes a fundamental change in bulk composition of the system prior to crystallization of domain 3 monazite and inclusion into Grt₁ (e.g. low-Th rim on grain 05G-019B-XZ-m6 in Figs 6a & 13d). This change is most readily explained by episodic or wholesale melt loss that left little Th behind in the residue for incorporation into domain 3 monazite (stage 4 in Fig. 15; see also Baldwin et al., 2006). Thus, melt extraction preceded or coincided with crystallization of domain 3 monazite in samples 04G-097 and 05G-019B $(2587 \pm 39 \text{ to } 2514 \pm 47 \text{ Ma}, 2\sigma; \text{ Table S4})$. The occurrence of domain 3 monazite in low-grossular Grt₁ cores (Fig. 6a) and high-grossular Grt₁ annuli (Figs 12a,b & 13e) implies that melt extraction was episodic during Neoarchean prograde loading from <0.8 to >1.4 GPa (Fig. 16). These results also suggest that Th-zoning in monazite from anatectic rocks may provide constraints on the timing of melt migration in orogenic systems (e.g. Lederer *et al.*, 2013).

Eu-anomalies in monazite

Positive Eu-anomalies in monazite are rare (Fig. S7; see Krenn *et al.*, 2008; Dumond *et al.*, 2010 for examples). A review of the literature for which Eu data are reported suggests monazite typically contains <2300 ppm Eu and commonly exhibits negative Eu-anomalies on chondrite-normalized REE plots (Bea *et al.*, 1994; Bea, 1996; Hermann & Rubatto, 2003; Kelly *et al.*, 2006; Rubatto *et al.*, 2006). Most monazite domains in this study display positive Eu-anomalies with Eu varying from 3092 to 4850 ppm,

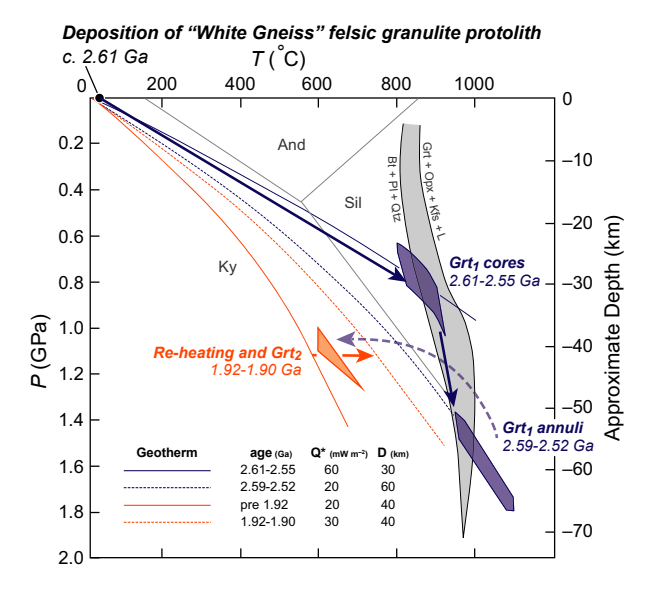


Fig. 16. P-T-t path for the Upper Deck felsic granulite based on this study. Calculated geothermal gradients are shown for comparison for a variety of crustal thicknesses (D) and mantle heat fluxes (Q^*) . The fluid-absent biotite melting field is reproduced from Vielzeuf & Montel (1994). See text for discussion.

and several domains are below detection for Sm (Table S5). Positive Eu-anomalies in monazite may be caused by incorporation of excess Eu into the monazite structure synchronous with breakdown of a Eu-bearing phase like plagioclase, K-feldspar or apatite. Monazite may also acquire a positive Eu-anomaly due to depletion of available Sm + Gd in the system during crystallization of a modally abundant (Sm + Gd)-bearing phase such as garnet.

Trace element studies reveal that granulite facies garnet generally has high $Sm_{(N)}/Gd_{(N)}$, compared to amphibolite-grade garnet (where(N) = normalized relative to chondrite; review by Jung & Hellebrand, 2006). Granulite-grade garnet is also generally more enriched in Sm + Gd (13.2 ppm Sm and 18.5 ppm Gd for garnet granulites reported by Bea & Montero, 1999). Modally abundant garnet could potentially exert a strong influence on the available reservoir of Sm + Gd + HREEs in high-grade systems. Bea & Montero (1999) observed a progressive depletion of middle REEs (Sm + Gd) and HREEs in monazite with increasing metamorphic grade and modal abundance of garnet, based on work in the Ivrea–Verbano Kinzigite Formation. We suggest that part of the explanation for positive Eu-anomalies in monazite in UHT felsic granulites of this study is due to the fact that monazite grew in the presence of modally abundant garnet that sequestered Sm + Gd.

Positive Eu-anomalies in lower crustal monazite are further explained by evidence for breakdown of Eu-bearing phases like apatite and/or plagioclase, in this case as reactants during fluid-absent melting of

Bt + Pl + Qtz. Textural evidence for dissolution of apatite (e.g. rounded grains included in garnet in Fig. 6a) and its absence from the felsic granulite matrix implies that it may have contributed Ca and Eu to domain 2 during melting and subsequent monazite crystallization. However, domain 3 monazite grains are Ca- and Th-depleted and inferred to have grown during episodic melt extraction in the absence of apatite. Domain 3 is characterized by some of the highest positive Eu-anomalies with absolute abundances of Eu up to 4850 ppm (Fig. S8b; Table S5). Some of these grains also occur in the high-grossular annuli of Grt₁ (Figs 12a,b & 13e) which locally preserve the resorbed reactants of partial melting (Bt + Pl inclusions in Figs 5e & 12a,b). We attribute the large positive Eu-anomalies for domain 3 to both an increase in the modal abundance of granulite-grade garnet (sequestering Sm + Gd) and simultaneous breakdown of plagioclase (liberating Eu for incorporation into monazite and Ca for incorporation into garnet; stage 4 in Fig. 15). Domain 3 monazite is interpreted as a physical record of plagioclase breakdown and HP grossular-rich garnet growth culminating with UHT-HP conditions in the Neoarchean (Figs 15 & S8c).

Monazite as a monitor of feldspar recrystallization

Domain 4 monazite grains are characterized by distinct LREE enrichment, particularly La + Ce (Fig. S8a: Table S5). Much of domain 4 is also associated with recrystallized ternary feldspar or plagioclase in the matrix (Figs 12c,d, 13h & 14a), and some are intergrown with or included in low-grossular garnet rims (e.g. Grt₂ rims of sample 05G-019B; Fig. 13f,g; stage 5 in Fig. 15). The weighted mean age of 1913 ± 25 Ma $(2\sigma, MSWD = 0.1)$ for five domain 4 grains in sample 05G-019B constrains the timing of Grt₂ growth based on inclusion and intergrowth of the grains in Grt₂ rims (Fig. S8c). Dates for elongated and asymmetric overgrowths of Domain 4 monazite in 04G-097 and 05G-026B constrain the timing of dextral shearing in the Upper Deck domain to c. 1.92-1.90 Ga (Figs 12d, 14b & S8c).

Feldspar in granulites is typically highly enriched in LREEs, particularly La + Ce (Bea, 1996; Villaseca et al., 2003). The marked enrichment in La + Ce observed in domain 4 monazite (relative to all other domains plotted in Fig. S8a) is most consistent with incorporation of La + Ce during recrystallization of feldspar. The observation of prominent Eu-anomalies in domain 4 monazite (Fig. S8b; Table S5) is consistent with dissolution–re-precipitation of pre-existing high Eu domain 3 monazite during sub-solidus growth of low-grossular Grt₂ at the expense of plagioclase (stage 5 in Fig. 15). One possible interpretation is that feldspar recrystallization and growth of Grt₂ concurrent with monazite dissolution–re-precipitation

was facilitated by emplacement of the c. 1.9 Ga Robillard granite along the western boundary of the Upper Deck (Fig. 2). Re-heating during dextral strain along the Algold Bay shear zone would have enabled production of the syn-tectonic Grt₂ coronas around Opx in 04G-097 (Fig. 5c), a process inferred by Williams et al. (2014) to explain repeated growth of garnet in lower crustal felsic orthogneisses. Mobilization of alkaline fluids derived from the Robillard granite would also have enhanced fluid-mediated partial alteration of monazite (Hetherington & Harlov, 2008; Harlov et al., 2011). Further research is necessary to understand the relative roles of dislocation creep v. dissolution-precipitation creep as mechanisms for recrystallizing feldspar and precipitating domain 4 monazite in these otherwise dry felsic granulites at c. 1.92-1.90 Ga (e.g. Wawrzenitz et al., 2012).

Felsic granulite P-T-t path and regional implications for the Athabasca granulite terrane

Figure 16 illustrates the P-T-t path inferred for Upper Deck felsic granulites based on results from this study. Prograde loading and burial of the metasedimentary protolith was followed by melting and growth of low-grossular peritectic garnet at 0.6-0.8 GPa and >800 °C at c. 2.61–2.55 Ga (Fig. 16). Melting in excess of 950 °C was facilitated by emplacement of the Upper Deck mafic sill complex, concurrent with crustal thickening and growth of high-grossular garnet annuli at >1.4 GPa at c. 2.59-2.52 Ga (Fig. 16). The record of UHT metamorphism in the Upper Deck associated with abundant mafic granulite sills supports its interpretation as an exposed deep crustal 'hot zone' (e.g. Annen et al., 2006). In this case, UHT metamorphism and partial melting of lower crust was facilitated by under- and intra-plating of mantle-derived magma in the Neoarchean.

Results from this study are in stark contrast to data from mafic granulite gneisses and eclogite layers hosted within the felsic granulites of the Upper Deck domain that are interpreted to represent the effects of HP metamorphism at c. 1.9 Ga, despite also containing zircon dated at c. 2.54-2.52 Ga (Baldwin et al., 2003, 2004). We suggest that Neoarchean zircon dates from the mafic granulite and eclogite gneisses represent metamorphic growth associated with the culmination of UHT-HP metamorphism identified in the felsic granulite gneisses in this study and consistent with the work of Snoeyenbos et al. (1995) and Baldwin et al. (2006). This suggestion is supported by recent work on poly-metamorphic mafic and felsic granulites in the adjoining Northwestern and Chipman domains that record c. 2.60–2.55 Ga HP metamorphism and lower crustal sub-horizontal fabric development that may have been coeval (Flowers et al., 2008; Mahan et al., 2008; Dumond et al., 2010; Regan *et al.*, 2014). This interpretation implies a regional-scale (100s of km²) Neoarchean record of HP metamorphism (<0.8 to \geq 1.4 GPa) concurrent with crustal thickening, intra-plating of mafic magmas, and lower crustal flow in all three domains of the EAmt (Fig. 1b).

Work in the Chipman domain supports long-term lower crustal residence for portions of the Athabasca granulite terrane at c. 2.55-1.9 Ga (Williams & Hanmer, 2006; Flowers et al., 2008; Mahan et al., 2008). Our results are similar to data from felsic granulites in the Northwestern domain (Fig. 1b) that record two distinct episodes of monazite growth in the Neoarchean and Paleoproterozoic, separated by an inferred period of isobaric cooling (Dumond et al., 2010; Regan et al., 2014). The dashed retrograde path in Fig. 16 represents our interpretation for the fate of the Neoarchean Upper Deck, such that rocks cooled to an ambient crustal geotherm after UHT-HP crustal thickening. The c. 1.9 Ga sub-solidus growth of a second generation of garnet in both 04G-097 and 05G-019B is most consistent with re-heating and crustal reactivation during dextral transpression at c. 1.92–1.90 Ga (Fig. 16; Dumond et al., 2008). The concordant Robillard pluton (Hanmer et al., 1994; Fig. 2) and the cross-cutting granite dyke dated by Baldwin et al. (2006) are evidence for this c. 1.9 Ga re-heating event in the vicinity of the Upper Deck. Flowers et al. (2006, 2008) dated the c. 1.9 Ga record of re-heating in the adjoining Chipman domain that was facilitated by the Chipman mafic dyke swarm (Williams et al., 1995). Dextral reactivation and feldspar recrystallization apparently affected large portions of the Athabasca granulite terrane at c. 1.9 Ga, including the EAmt and domains west of the Grease River shear zone that were all affected by the c. 1.94–1.90 Ga west-vergent Taltson arc-continent collision (Fig. 2: Dumond et al., 2008, 2010: Bethune et al., 2013; Regan et al., 2014).

CONCLUSIONS

Monazite in continental lower crust represents a potentially powerful monitor of partial melting, melt transfer, garnet growth and feldspar recrystallization. Monazite grains in this study are marked by positive Eu-anomalies relative to chondrite. The results suggest a direct link between Y, Sm, Eu and Gd in monazite and the behaviour of two major phases in continental lower crust-garnet and plagioclase. Positive Eu-anomalies in lower crustal monazite associated with modally abundant garnet appear to be directly related to depletions of Y, Sm and Gd in monazite during/after garnet growth and enrichments of Eu (and La + Ce) in monazite during loss or recrystallization of plagioclase. Our results from residual UHT-HP felsic granulites validate recent laboratory results that suggest monazite solubility is greatly reduced at high pressure (Stepanov et al., 2012), although melt composition may still exert an important control on this behaviour (Montel, 1993).

ACKNOWLEDGEMENTS

C. Yakymchuk and P. Pitra are acknowledged for helpful and thorough reviews. Editor M. Brown is thanked for outstanding guidance during the revision process. Discussions with C. L. Andronicos, J. A. Baldwin, K. H. Mahan, K. Schulmann and D. R. Snoeyenbos are greatly appreciated. C. L. Andronicos first suggested we normalize the protolith bulk composition to a shale or greywacke bulk composition to test for a sedimentary precursor. Stereonets were produced with GEOrient v. 9.5.0. Funding for this research was provided by NSF-EAR grants 0310004, 0609935 and 1255277. P. Goncalves acknowledges the 'défi NEEDS' from the INSU-CNRS (France) for travel support and monazite research funding. Additional funding was provided by a 2006 Mineralogical Society of America Grant for Student Research in Mineralogy and Petrology to G. Dumond. Financial support for fieldwork was also provided by the Leo Hall and Gloria Radke Memorial Funds (Department of Geosciences. University of Massachusetts) and the University of Arkansas.

REFERENCES

- Annen, C., Blundy, J.D. & Sparks, S.J., 2006. The genesis of intermediate and silicic magmas in deep crustal hot zones. Journal of Petrology, 47, 505-539.
- Baldwin, J.A., Bowring, S.A. & Williams, M.L., 2003. Petrological and geochronological constraints on high pressure, high temperature metamorphism in the Snowbird tectonic zone, Canada. Journal of Metamorphic Geology, 21, 81-98.
- Baldwin, J.A., Bowring, S.A., Williams, M.L. & Williams, I.S., 2004. Eclogites of the Snowbird tectonic zone: petrological and U-Pb geochronological evidence for Paleoproterozoic high-pressure metamorphism in the western Canadian Shield. Contributions to Mineralogy and Petrology, **147,** 528–548.
- Baldwin, J.A., Bowring, S.A., Williams, M.L. & Mahan, K.H., 2006. Geochronological constraints on the evolution of highpressure felsic granulites from an integrated electron microprobe and ID-TIMS geochemical study. Lithos, 88, 173–200.
- Baldwin, J.A., Powell, R., Williams, M.L. & Goncalves, P., 2007. Formation of eclogite, and reaction during exhumation to mid-crustal levels, Snowbird tectonic zone, western Canadian Shield. Journal of Metamorphic Geology, 25, 953-974.
- Baldwin, J.A., Powell, R., White, R.W. & Stípská, P., 2015. Using calculated chemical potential relationships to account for replacement of kyanite by symplectite in high pressure granulites. Journal of Metamorphic Geology, 33, 311-330.
- Bea, F., 1996. Residence of REE, Y, Th, and U in granites and crustal protoliths: implications for the chemistry of crustal melts. Journal of Petrology, 37, 521-552.
- Bea, F. & Montero, P., 1999. Behavior of accessory phases and redistribution of Zr, REE, Y, Th, and U during metamorphism and partial melting of metapelites in the lower crust: an example from the Kinzigite Formation of Ivrea-Verbano, NW Italy. Geochimica et Cosmochimica Acta, 63, 1133-1153.
- Bea, F., Pereira, M.D. & Stroh, A., 1994. Mineral-leucosome trace element partitioning in a peraluminous migmatite (a

- laser ablation-ICP-MS study). Chemical Geology, 117, 291-312.
- Beaumont, C., Jamieson, R.A., Nguyen, M.H. & Lee, B., 2001. Himalayan tectonics explained by extrusion of a lowviscosity crustal channel coupled to focused surface denudation. Nature, 414, 738-742.
- Beaumont, C., Jamieson, R.A., Nguyen, M.H. & Medvedev, S., 2004. Crustal channel flows: 1. Numerical models with applications to the tectonics of the Himalayan-Tibetan orogen. Journal of Geophysical Research-Solid Earth, 109, 1–29. doi:10.1029/2003ib002809.
- Bethune, K.M., Berman, R.G., Rayner, N. & Ashton, K.E., 2013. Structural, petrological and U-Pb SHRIMP geochronological study of the western Beaverlodge domain: implications for crustal architecture, multi-stage orogenesis and the extent of the Taltson orogen in the SW Rae craton, Canadian Shield. Precambrian Research, 232, 89-118.
- Brown, M., 2002. Retrograde processes in migmatites revisited. Journal of Metamorphic Geology, 20, 25-40.
- Brown, M. & Solar, G.S., 1998. Shear-zone systems and melts: feedback relations and self-organization in orogenic belts. Journal of Structural Geology, 20, 211–227. Bucher, K. & Frey, M., 2002. Petrogenesis of Metamorphic
- Rocks. Springer, Berlin, 341 pp.
- Carswell, D.A. & O'Brien, P.J., 1993. Thermobarometry and geotectonic significance of high-pressure granulites: examples from the Moldanubian zone of the Bohemian Massif in lower Austria. Journal of Petrology, 34, 427-459.
- Chen, Y., Ye, K., Liu, J.-B. & Sun, M., 2008. Quantitative P-T-X constraints on orthopyroxene-bearing high-pressure granulites in felsic-metapelitic rocks: evidence from the Huangtuling granulite, Dabieshan Orogen. Journal of Metamorphic Geology, 26, 1–15.
- Clemens, J.D., 2006. Melting of the continental crust: fluid regimes, melting reactions, and source-rock fertility. In: Evolution and Differentiation of the Continental Crust (eds Brown, M. & Rushmer, T.), pp. 296–327. Cambridge University Press, Cambridge.
- Clemens, J.D. & Vielzeuf, D., 1987. Constraints on melting and magma production in the crust. Earth and Planetary Science Letters, 86, 287-306.
- Coggon, R. & Holland, T.J.B., 2002. Mixing properties of phengitic micas and revised garnet-phengite thermobarometers. Journal of Metamorphic Geology, 20, 683–696.
- Condie, K.C., 1993. Chemical composition and evolution of the upper continental crust: contrasting results from surface samples and shales. Chemical Geology, 104, 1-37.
- Connolly, J.A.D., 2005. Computation of phase equilibria by linear programming: a tool for geodynamic modeling and its application to subduction zone decarbonation. Earth and Planetary Science Letters, 236, 524-541.
- Crowley, J.L., Waters, D.J., Searle, M.P. & Bowring, S.A., 2009. Pleistocene melting and rapid exhumation of the Nanga Parbat massif, Pakistan: age and P-T conditions of accessory mineral growth in migmatite and leucogranite. Earth and Planetary Science Letters, 288, 408-420.
- Donovan, J.J., Snyder, D.A. & Rivers, M.L., 1993. An improved interference correction for trace element analysis. Microbeam Analysis, 2, 23-28.
- Dumond, G., McLean, N., Williams, M.L., Jercinovic, M.J. & Bowring, S.A., 2008. High-resolution dating of granite petrogenesis and deformation in a lower crustal shear zone: Athabasca granulite terrane, western Canadian Shield. Chemical Geology, 254, 175-196.
- Dumond, G., Goncalves, P., Williams, M. L. & Jercinovic, M. J., 2010. Sub-horizontal fabric in exhumed continental lower crust and implications for lower crustal flow: Athabasca granulite terrane, western Canadian Shield. Tectonics, 29, TC2006. doi:10.1029/2009TC002514.
- Dumond, G., Mahan, K.H., Williams, M.L. & Jercinovic, M.J., 2013. Transpressive uplift and exhumation of continental

- lower crust revealed by synkinematic monazite reactions. *Lithosphere*, **5**, 507–512.
- Fiala, J., Matějovská, O. & Vaňková, V., 1987. Moldanubian granulites: source material and petrogenetic considerations. Neues Jahrbuch für Mineralogie Abhandlungen, 157, 133–165.
- Flowers, R., Bowring, S. & Williams, M., 2006. Timescales and significance of high-pressure, high-temperature metamorphism and mafic dike anatexis, Snowbird tectonic zone, Canada. *Contributions to Mineralogy and Petrology*, **151**, 558–581.
- Flowers, R.M., Bowring, S., Mahan, K.H. & Williams, M.L., 2008. Stabilization and reactivation of cratonic lithosphere from the lower crustal record in the western Canadian shield. *Contributions to Mineralogy and Petrology*, **156**, 529–549.
- Foster, G., Gibson, H.D., Parrish, R., Horstwood, M., Fraser, J. & Tindle, A., 2002. Textural, chemical and isotopic insights into the nature and behaviour of metamorphic monazite. *Chemical Geology*, **191**, 183–207.
- Foster, G., Parrish, R.R., Horstwood, M.S.A., Chenery, S., Pyle, J. & Gibson, H.D., 2004. The generation of prograde P-T-t points and paths; a textural, compositional, and chronological study of metamorphic monazite. *Earth and Planetary Science Letters*, **228**, 125–142.
- Frost, B.R., Barnes, C.G., Collins, W.J., Arculus, R.J., Ellis, D.J. & Frost, C.D., 2001. A geochemical classification for granitic rocks. *Journal of Petrology*, 42, 2033–2048.
- Fuhrman, M.L. & Lindsley, D.H., 1988. Ternary-feldspar modeling and thermometry. *American Mineralogist*, 73, 201– 215.
- Gasquet, D., Bertrand, J.-M., Paquette, J.-L. et al., 2010. Miocene to Messinian deformation and hydrothermal activity in a pre-Alpine basement massif of the French western Alps: new U-Th-Pb and Ar ages from the Lauzière massif. Bulletin de la Société Géologique de France, 181, 227-241.
- Gibson, H.D., Carr, S.D., Brown, R.L. & Hamilton, M.A., 2004. Correlations between chemical and age domains in monazite, and metamorphic reactions involving major pelitic phases: an integration of ID-TIMS and SHRIMP geochronology with Y-Th-U X-ray mapping. *Chemical Geology*, 211, 237–260.
- Goncalves, P., Nicollet, C. & Montel, J.-M., 2004. Petrology and in situ U-Th-Pb monazite geochronology of ultrahightemperature metamorphism from the Andriamena mafic unit, North-Central Madagascar. Significance of a petrographical P-T path in a polymetamorphic context. *Journal* of Petrology, 45, 1923–1957.
- Green, D.H. & Lambert, I.B., 1965. Experimental crystallization of anhydrous granite at high pressures and temperatures. *Journal of Geophysical Research*, 70, 5259–5268.
- Green, E.C.R., Holland, T.J.B. & Powell, R., 2007. An order–disorder model for omphacitic pyroxenes in the system jadeite–diopside–hedenbergite–acmite, with applications to eclogite rocks. *American Mineralogist*, **92**, 1181–1189.
- Hanmer, S., 1994. Geology, East Athabasca Mylonite Triangle, Saskatchewan: Map 1859A, Scale 1:100000. Geological Survey of Canada, Ottawa.
- Hanmer, S., 1997. Geology of the Striding-Athabasca mylonite zone, northern Saskatchewan and southeastern District of Mackenzie, Northwest Territories. Geological Survey of Canada Bulletin, 501, 92 pp.
- Hanmer, S., Parrish, R.R., Williams, M.L. & Kopf, C., 1994.
 Striding-Athabasca mylonite zone: complex Archean deep crustal deformation in the East Athabasca mylonite triangle,
 N. Saskatchewan. Canadian Journal of Earth Sciences, 31, 1287–1300.
- Hanmer, S., Williams, M.L. & Kopf, C., 1995. Modest movements, spectacular fabrics in an intracontinental deep-crustal strike-slip fault: striding-Athabasca mylonite zone, NW Canadian Shield. *Journal of Structural Geology*, 17, 493–507.
- Harlov, D.E., Wirth, R. & Hetherington, C.J., 2011. Fluid-mediated partial alteration in monazite: the role of coupled

- dissolution-reprecipitation in element redistribution and mass transfer. Contributions to Mineralogy and Petrology, 162, 329-348
- Hermann, J. & Rubatto, D., 2003. Relating zircon and monazite domains to garnet growth zones: age and duration of granulite facies metamorphism in the Val Malenco lower crust. *Journal of Metamorphic Geology*, **21**, 833–852.
- Hetherington, C.J. & Harlov, D.E., 2008. Metasomatic thorite and uraninite inclusions in xenotime and monazite from granitic pegmatites, Hidra anorthosite massif, southwestern Norway: mechanics and fluid chemistry. *American Mineralogist*, **93**, 806–820.
- Holland, T.J.B. & Powell, R., 1998. An internally consistent thermodynamic data set for phases of petrological interest. *Journal of Metamorphic Geology*, **16**, 309–343.
- Hollister, L.S. & Crawford, M.L., 1986. Melt-enhanced deformation: a major tectonic process. *Geology*, 14, 558–561.
- Jercinovic, M.J. & Williams, M.L., 2005. Analytical perils (and progress) in electron microprobe trace element analysis applied to geochronology: background acquisition, interferences, and beam irradiation effects. *American Mineralogist*, **90.** 526–546.
- Jercinovic, M.J., Williams, M.L. & Lane, E.D., 2008. In-situ trace element analysis of monazite and other fine-grained accessory minerals by EPMA. *Chemical Geology*, 254, 197– 215.
- Johnson, T.E., White, R.W. & Powell, R., 2008. Partial melting of metagreywacke: a calculated mineral equilibria study. *Journal of Metamorphic Geology*, 26, 837–853.
 Jung, S. & Hellebrand, E., 2006. Trace element fractionation
- Jung, S. & Hellebrand, E., 2006. Trace element fractionation during high-grade metamorphism and crustal melting—constraints from ion microprobe data of metapelitic, migmatitic and igneous garnets and implications for Sm-Nd garnet chronology. *Lithos*, 87, 193–213.
- Kelly, N.M., Clarke, G.L. & Harley, S.L., 2006. Monazite behaviour and age significance in poly-metamorphic high-grade terrains: a case study from the western Musgrave Block, central Australia. *Lithos*, **88**, 100–134.
- Kelsey, D.E. & Hand, M., 2015. On ultrahigh temperature crustal metamorphism: Phase equilibria, trace element thermometry, bulk composition, heat sources, timescales, and tectonic settings. *Geoscience Frontiers*, **6**, 311–356. doi:10.1016/j.gsf. 2014.09.006.
- Kelsey, D.E., Clark, C. & Hand, M., 2008. Thermobarometric modelling of zircon and monazite growth in melt-bearing systems: examples using model metapelitic and metapsammitic granulites. *Journal of Metamorphic Geology*, **26**, 199–212.
- Keppler, H. & Wyllie, P.J., 1990. Role of fluids in transport and fractionation of uranium and thorium in magmatic processes. *Nature*, 348, 531–533.
- Kohn, M.J., Wieland, M.S., Parkinson, C.D. & Upreti, B.N., 2005. Five generations of monazite in Langtang gneisses: implications for chronology of the Himalayan metamorphic core. *Journal of Metamorphic Geology*, **23**, 399–406.
- Kopf, C.F., 1999. Deformation, Metamorphism, and Magmatism in the East Athabasca Mylonite Triangle, Northern Saskatchewan: Implications for the Archean and Early Proterozoic Crustal Structure of the Canadian Shield. Unpublished thesis, University of Massachusetts, Amherst, MA, 156 pp.
- Korhonen, F.J., Brown, M., Clark, C. & Bhattacharya, S. 2013. Osmulite-melt interactions in ultrahigh temperature granulites: phase equilibria modelling and implications for the *P-T-t* evolution of the Eastern Ghats Province, India. *Journal of Metamorphic Geology*, 31, 881–907.
 Korhonen, F.J., Clark, C., Brown, M. & Taylor, R.J.M., 2014.
- Korhonen, F.J., Clark, C., Brown, M. & Taylor, R.J.M., 2014. Taking the temperature of earth's hottest crust. *Earth and Planetary Science Letters*, **408**, 341–354.
- Planetary Science Letters, 408, 341–354. Krenn, E., Putz, H., Finger, F. & Paar, W., 2008. Unusual monazite with high S, Sr, Eu, and common Pb contents in ore bearing mylonites from the Schellgaden mining district,

- Austria. Geophysical Research Abstracts, 10, EGU2008-A-11796.
- Krikorian, L., 2002. Geology of the Wholdaia Lake segment of the Snowbird Tectonic Zone, Northwest Territories (Nunavut): A View of the Deep Crust During Assembly and Stabilization of the Laurentian craton. Unpublished MS thesis, University of Massachusetts, Amherst, MA, 90 pp.
- Lederer, G.W., Cottle, J.M., Jessup, M.J., Langille, J.M. & Ahmad, T., 2013. Timescales of partial melting in the Himalayan middle crust: insight from the Leo Pargil dome, northwest India. Contributions to Mineralogy and Petrology, 166, 1415–1441.
- Mahan, K.H. & Williams, M.L., 2005. Reconstruction of a large deep-crustal terrane: implications for the Snowbird tectonic zone and early growth of Laurentia. *Geology*, 33, 385– 388.
- Mahan, K.H., Williams, M.L. & Baldwin, J.A., 2003. Contractional uplift of deep crustal rocks along the Legs Lake shear zone, western Churchill Province, Canadian Shield. *Canadian Journal of Earth Sciences*, **40**, 1085–1110.
- Mahan, K.H., Goncalves, P., William, M.L. & Jercinovic, M.J., 2006a. Dating metamorphic reactions and fluid flow: application to exhumation of high-P granulites in a crustalscale shear zone, western Canadian Shield. *Journal of Metamorphic Geology*, 24, 193–217.
- Mahan, K.H., Williams, M.L., Flowers, R.M., Jercinovic, M.J., Baldwin, J.A. & Bowring, S.A., 2006b. Geochronological constraints on the Legs Lake shear zone with implications for regional exhumation of lower continental crust, western Churchill Province, Canadian Shield. *Contributions to Mineralogy and Petrology*, **152**, 223–242.
- Mahan, K.H., Goncalves, P., Flowers, R., Williams, M.L. & Hoffman-Setka, D., 2008. The role of heterogeneous strain in the development and preservation of a polymetamorphic record in high-*P* granulites, western Canadian Shield. *Journal of Metamorphic Geology*, **26**, 669–694.
- Mahan, K.H., Smit, C.A., Williams, M.L., Dumond, G. & van Reenen, D.D., 2011. Heterogeneous strain and polymetamorphism in high-grade terranes: insight into crustal processes from the Athabasca Granulite Terrane, western Canada, and the Limpopo Complex, southern Africa. In: Origin and Evolution of High-grade Gneiss Terranes, with Special Emphasis on the Limpopo Complex of Southern Africa (eds van Reenen, D.D., Kramers, J.D., McCourt, S. & Perchuk, L.L.), Geological Society of America Memoir, 207, 269–287.
- Martel, E., van Breemen, O., Berman, R.G. & Pehrsson, S., 2008. Geochronology and tectonometamorphic history of the Snowbird Lake area, Northwest Territories, Canada: new insights into the architecture and significance of the Snowbird tectonic zone. *Precambrian Research*, **161**, 201–230.
- Martins, L., Vlach, S.R.F. & Janasi, V., 2009. Reaction microtextures of monazite: correlation between chemical and age domains in the Nazaré Paulista migmatite, SE Brazil. *Chemical Geology*, 261, 271–285.
 Montel, J.M., 1986. Experimental determination of the solubil-
- Montel, J.M., 1986. Experimental determination of the solubility of Ce-monazite in SiO₂–Al₂O₃–K₂O–Na₂O melts at 800°C, 2 kbar, under H₂O-saturated conditions. *Geology*, **14**, 659–662.
- Montel, J.-M., 1993. A model for monazite/melt equilibrium and application to the generation of granitic magmas. *Chemical Geology*, **110**, 127–146.
- O'Brien, P.J. & Rötzler, J., 2003. High-pressure granulites: formation, recovery of peak conditions and implications for tectonics. *Journal of Metamorphic Geology*, **21**, 3–20.
- Pyle, J.M. & Spear, F.S., 2003. Four generations of accessory-phase growth in low-pressure migmatites from SW New Hampshire. *American Mineralogist*, **88**, 338–351.
- Pyle, J.M., Spear, F.S., Rudnick, R.L. & McDonough, W.F., 2001. Monazite-xenotime-garnet equilibrium in metapelites and a new monazite-garnet thermometer. *Journal of Petrol*ogy, 42, 2083–2107.

- Pyle, J.M., Spear, F.S. & Wark, D.A., 2002. Electron microprobe analysis of REE in Apatite, monazite, and xenotime: protocols and pitfalls. In: *Reviews in Mineralogy and Geochemistry* (eds Kohn, M.J., Rakovan, J. & Hughes, J.M.), pp. 337–362. Mineralogical Society of America, Washington, DC.
- Pyle, J.M., Spear, F.S., Wark, D.A., Daniel, C.G. & Storm, L.C., 2005. Contributions to precision and accuracy of chemical ages of monazite. *American Mineralogist*, **90**, 547–577
- Rapp, R.P. & Watson, E.B., 1986. Monazite solubility and dissolution kinetics: implications for the Th and light rare-earth chemistry of felsic magmas. *Contributions to Mineralogy and Petrology*, 94, 304–316.
- Rapp, R.P., Ryerson, F.J. & Miller, C.F., 1987. Experimental evidence bearing on the stability of monazite during crustal anatexis. *Geophysical Research Letters*, 14, 307–310.
- Regan, S., Williams, M.L., Mahan, K.H., Leslie, S., Jercinovic, M.J. & Holland, M.E., 2014. The Cora Lake shear zone, Athabasca granulite terrane: an intraplate response to far-field orogenic processes during the amalgamation of Laurentia. Canadian Journal of Earth Sciences, 51, 877–901.
- Reno, B.L., Piccoli, P.M., Brown, M. & Trouw, R.A.J., 2012. In situ monazite (U–Th)–Pb ages from the Southern Brasilia Belt, Brazil: constraints on the high-temperature retrograde evolution of HP granulites. *Journal of Metamorphic Geology*, 30, 81–112.
- Rosenberg, C.L. & Handy, M.R., 2005. Experimental deformation of partially melted granite revisited: implications for the continental crust. *Journal of Metamorphic Geology*, 23, 19–28.
- Rubatto, D., Hermann, J. & Buick, I.S., 2006. Temperature and bulk composition control on the growth of monazite and zircon during low-pressure anatexis (Mount Stafford, central Australia). *Journal of Petrology*, 47, 1973–1996.
- Rudnick, R.L., 1992. Restites, Eu-anomalies, and the lower continental crust. Geochimica et Cosmochimica Acta, 56, 963–970.
- Rudnick, R.L. & Gao, S., 2003. Composition of the continental crust. In: *Treatise on Geochemistry* (eds Holland, H.D. & Turekian, K.K.), Vol. 3, pp. 1–64. Elsevier, Oxford.
- Searle, M., 2013. Crustal melting, ductile flow, and deformation in mountain belts: cause and effect relationships. *Lithosphere*, 5, 547–554.
- Skora, S. & Blundy, J., 2012. Monazite solubility in hydrous silicic melts at high pressure conditions relevant to subduction zone metamorphism. Earth and Planetary Science Letters, 321–322, 104–114.
- Slimmon, W.L., 1989. Bedrock compilation geology Fond du Lac (NTS 74–O): Map 247A, scale 1:250000, Saskatchewan Geological Survey, Saskatchewan Energy and Mines.
 Snoeyenbos, D.R., Williams, M.L. & Hanmer, S., 1995.
- Snoeyenbos, D.R., Williams, M.L. & Hanmer, S., 1995. Archean high-pressure metamorphism in the western Canadian Shield. *European Journal of Mineralogy*, 7, 1251–1272.
- Spear, F.S. & Kohn, M.J., 1996. Trace element zoning in garnet as a monitor of crustal melting. *Geology*, **24**, 1099–1102.
- Stepanov, A.S., Hermann, J., Rubatto, D. & Rapp, R.P., 2012. Experimental study of monazite/melt partitioning with implications for the REE, Th and U geochemistry of crustal rocks. *Chemical Geology*, 300–301, 200–220.
- Štípská, P. & Powell, R., 2005. Does ternary feldspar constrain metamorphic conditions of high-grade meta-igneous rocks? Evidence from orthopyroxene granulites, Bohemian Massif. *Journal of Metamorphic Geology*, **23**, 627–647.
- Sun, S.-S. & McDonough, W.F., 1989. Chemical and isotope systematics of oceanic basalts: implications for mantle compositions and processes. In: *Magmatism in the Ocean Basins* (eds Saunders, A.D. & Norry, M.J.), pp. 313–345. Geological Society, London.
- Tajčmanová, L., Connolly, J.A.D. & Cesare, B., 2009. A ther-modynamic model for titanium and ferric iron solution in biotite. *Journal of Metamorphic Geology*, 27, 153–165.
- Tropper, P., Knozett, J. & Finger, F., 2005. Experimental constraints on the formation of high-P/high-T granulites in the

- Southern Bohemian Massif. European Journal of Mineralogy, 17, 343-356.
- Vielzeuf, D. & Montel, J.M., 1994. Partial melting of metagreywackes. Part I. Fluid-absent experiments and phase relationships. *Contributions to Mineralogy and Petrology*, 117, 375–393.
- Vielzeuf, D. & Schmidt, M.W., 2001. Melting relations in hydrous systems revisited: application to metapelites, metagreywackes and metabasalts. Contributions to Mineralogy and Petrology, 141, 251–267.
- Villaseca, C., Romera, C.M., De la Rosa, J. & Barbero, L., 2003. Residence and redistribution of REE, Y, Zr, Th and U during granulite-facies metamorphism: behaviour of accessory and major phases in peraluminous granulites of central Spain. Chemical Geology, 200, 293–323.
- Watt, G.R., 1995. High-thorium monazite-(Ce) formed during disequilibrium melting of metapelites under granulite-facies conditions. *Mineralogical Magazine*, **59**, 735–743.
- Watt, G.R. & Harley, S.L., 1993. Accessory phase controls on the geochemistry of crustal melts and restites produced during water-undersaturated partial melting. *Contributions to Mineralogy and Petrology*, **114**, 550–566.
- Wawrzenitz, N., Krohe, A., Rhede, D. & Romer, R.L., 2012. Dating rock deformation with monazite: the impact of dissolution precipitation creep. *Lithos*, **134–135**, 52–74.
- Weiss, C.S., 1803. Über die Gebirgsart des sächsischen Erzgebirges, welche unter dem Namen Weiss-Stein neuerlich bekannt gemacht worden ist. Neue Schriften der Gesellschaft naturforschender Freunde zu Berlin, 4, 342–366.
- White, R.W. & Powell, R., 2002. Melt loss and the preservation of granulite facies mineral assemblages. *Journal of Metamorphic Geology*, 20, 621–632.
- White, R.W., Powell, R., Holland, T.J.B. & Worley, B.A., 2000. The effect of TiO₂ and Fe₂O₃ on metapelitic assemblages at greenschist and amphibolite facies conditions: mineral equilibria calculations in the system K₂O–FeO–MgO–Al₂O₃–SiO₂–H₂O–TiO₂–Fe₂O₃. *Journal of Metamorphic Geology*, **18**, 497–511.
- White, R.W., Powell, R. & Holland, T.J.B., 2001. Calculation of partial melting equilibria in the system Na₂O–CaO–K₂O–FeO–MgO–Al₂O₃–SiO₂–H₂O (NCKFMASH). *Journal of Metamorphic Geology*, **19**, 139–153.
- White, R.W., Powell, R. & Halpin, J.A., 2004. Spatially-focused melt formation in aluminous metapelites from Broken Hill, Australia. *Journal of Metamorphic Geology*, **20**, 621–632.
- White, R.W., Powell, R. & Holland, T.J.B., 2007. Progress relating to calculation of partial melting equilibria for metapelites. *Journal of Metamorphic Geology*, **25**, 511–527.
- Williams, M.L. & Hanmer, S., 2006. Structural and metamorphic processes in the lower crust: evidence from a deep-crustal isobarically cooled terrane, Canada. In: *Evolution and Differentiation of the Continental Crust* (eds Brown, M. & Rushmer, T.), pp. 231–267. Cambridge University Press, Cambridge.
- Williams, M.L. & Jercinovic, M.J., 2002. Microprobe monazite geochronology: putting absolute time into microstructural analysis. *Journal of Structural Geology*, **24**, 1013–1028.
- Williams, M.L. & Jercinovic, M.J., 2012. Tectonic interpretation of metamorphic tectonites: integrating compositional mapping, microstructural analysis and *in situ* monazite dating. *Journal of Metamorphic Geology*, **30**, 739–752.
- Williams, M.L., Hanmer, S., Kopf, C. & Darrach, M., 1995. Syntectonic generation and segregation of tonalitic melts from amphibolite dikes in the lower crust, Striding-Athabasca mylonite zone, northern Saskatchewan. *Journal of Geophysical Research*, 100(B8), 15717–15734.
- Williams, M.L., Melis, E.A., Kopf, C. & Hanmer, S., 2000. Microstructural tectonometamorphic processes and the development of gneissic layering: a mechanism for metamorphic segregation. *Journal of Metamorphic Geology*, **18**, 41–57.
- Williams, M.L., Jercinovic, M.J., Goncalves, P. & Mahan, K., 2006. Format and philosophy for collecting, compiling, and

- reporting microprobe monazite ages. *Chemical Geology*, **225**, 1–15.
- Williams, M.L., Jercinovic, M.J. & Hetherington, C.J., 2007. Microprobe monazite geochronology: understanding geologic processes by integrating composition and chronology. Annual Review of Earth and Planetary Sciences, 35, 137–175.
- Williams, M.L., Karlstrom, K.E., Dumond, G. & Mahan, K.H., 2009. Perspectives on the architecture of continental crust from integrated field studies of exposed isobaric sections. Geological Society of America Special Papers, 456, 219–241.
- Williams, M.L., Dumond, G., Mahan, K.H., Regan, S.P. & Holland, M., 2014. Garnet-forming reactions in felsic orthogneiss: implications for densification and strengthening of the lower continental crust. Earth and Planetary Science Letters, 405, 207–219.
- Xing, L., Trail, D. & Watson, B.E., 2013. Th and U partitioning between monazite and felsic melt. *Chemical Geology*, **358**, 46–53
- Yakymchuk, C. & Brown, M., 2014a. Consequences of opensystem melting in tectonics. *Journal of the Geological Society*, 171, 21–40.
- Yakymchuk, C. & Brown, M., 2014b. Behaviour of zircon and monazite during crustal melting. *Journal of the Geological Society*, **171**, 465–479.
- Yakymchuk, C., Brown, M., Clark, C. et al., 2015. Decoding polyphase migmatites using geochronology and phase equilibria modeling. *Journal of Metamorphic Geology*, **33**, 203–230.
- Zhu, X.K. & O'Nions, R.K., 1999a. Monazite chemical composition: some implications for monazite geochronology. *Contributions to Mineralogy and Petrology*, **137**, 351–363.
- Zhu, X.K. & O'Nions, R.K., 1999b. Zonation of monazite in metamorphic rocks and its implications for high temperature thermochronology: a case study from the Lewisian terrain. *Earth and Planetary Science Letters*, **171**, 209–220.

SUPPORTING INFORMATION

Additional Supporting Information may be found in the online version of this article at the publisher's web site:

- **Figure S1.** Backscattered electron image of garnet in Opx-felsic granulite 04G-097. Note the abundant Fe-sulphide inclusions (pyrrhotite-Po) and associated inclusions of Bt + Pl + Rt. Ilmenite was notably absent in garnet porphyroblasts and only observed in the matrix.
- **Figure S2.** Plane-polarized light photomicrograph of garnet porphyroblast in (kyanite + sillimanite)-bearing felsic granulite 05G-019B illustrating rounded inclusions of quartz with graphite. Graphite also occurs as an abundant fabric-defining phase in the matrix.
- **Figure S3.** High-resolution full thin-section Ca $K\alpha$ map of D_2 ultramylonite sample 05G-026B illustrating setting of monazite grains (Fig. 14). Note the dextral sense of shear defined by fractured garnet porphyroclasts mantled by tails of quartz ribbons.
- **Figure S4.** Whole-rock geochemistry for Upper Deck felsic granulites and protolith from this study plotted with data from Baldwin *et al.* (2006). Compositions for greywacke (Condie, 1993; Vielzeuf & Montel, 1994), shale (Condie, 1993), high-pressure granite (Green & Lambert, 1965) and the Bohemian Massif felsic granulites (Fiala *et al.*, 1987; Carswell &